View metadata, citation and similar papers at core.ac.uk
brought to you by CORE
provided by CERN Document Server

LUNFD6/(NFFL-7121) 1996

Electron Identification with the ATLAS Detector at the Large Hadron Collider.[1]

Ulrik Egede
University of Lund
Institute of Physics
BOX 118
S - 221 00 Lund
Sweden.

April 8, 1996

Thesis for the degree of filosofie licentiat.

[1] http://www.quark.lu.se/activities/atlas/atlas.info/documentation/electronid.html

Abstract

For the ATLAS experiment at LHC identification of leptons will be of extreme importance. Here is presented the general physics motivation for electron identification together with the approach used in ATLAS. Special emphasis is put on the use of a transition radiation detector to improve the rejection of jets provided by the calorimeters and tracking alone. A general overview is given of how electron identification will be used in the physics analysis. The analysis of data from a prototype of the transition radiation tracker shows a detector which can work at a high luminosity hadron collider.

Contents

1 Preface **3**

2 Design of the ATLAS detector **5**
2.1 Overall Design 5
2.2 The muon system 8
2.3 The calorimeter 10
2.4 The inner detector 11
2.4.1 Precision tracking 12
2.4.2 Transition radiation tracker 12

3 Transition radiation **15**
3.1 Transition radiation from a single boundary 15
3.2 Radiators with many layers 17
3.3 N foils placed with regular spacing 21
3.4 Detection of X-rays 22
3.5 How to design a detector 23
3.6 Results from earlier transition radiation detectors 26

4 The 95 test of the endcap prototype **28**
4.1 Setup in the test beam 28
4.2 Frontend electronics for the prototype 30
4.3 Alignment 32
4.4 Purity 35
4.5 Electron identification 38
4.5.1 Dependence on detector length 43

5 Simulation and reconstruction **45**
5.1 Physics simulation 45
5.2 Detector simulation 45
5.3 Detector response 46
5.4 Triggering 46

5.5 Reconstruction 46
5.6 Pattern recognition and track fitting 47
5.7 Reconstruction of conversions 50
5.7.1 The vertex fit 50
5.7.2 The mass constraint fit 53
5.7.3 Photon from primary vertex 54

6 Physics potential of electron identification 55
6.1 B-physics 55
6.2 Conversions in the $H \to \gamma\gamma$ channel 58
6.3 Inclusive electron identification 62
6.4 Calibration of the EM calorimeter 66
6.4.1 The toy Monte Carlo 66
6.4.2 Time for calibration 68
6.5 b-tagging in $H \to b\bar{b}$ decays and top jets 69

7 Conclusion 74

A Glossary 76

Chapter 1

Preface

For the last many years new discoveries in particle physics have been dominated by the hadron colliders extending the energy range into virgin regions of particle physics. The last example of this is the discovery of the top quark at the Tevatron collider. The Large Hadron Collider, LHC, can be seen as the next step for hadron colliders and it will hopefully bring new understanding of our universe. LHC will be a proton-proton collider where the protons collide inside the detectors at a total energy of 14 TeV in the centre of mass system.

The theory for electroweak interactions had great success with the prediction and finally the discovery of the W and Z vector bosons at the SPS collider. In the electroweak theory it is however not sufficient with the four particles responsible for the electroweak interactions, the W^+, W^- and Z^0 massive vector bosons and the photon, since all particles in such a theory will be massless. The vector bosons can acquire mass by introducing a scalar doublet to break the symmetry between the four vector particles. By assigning each fermion a coupling to the scalar field proportional to the mass of the particle the same scalar field can describe the masses of all known particles.

With the scalar field, the Higgs field, there is associated a Higgs particle which, if discovered, will be a very strong proof for the mass creation theory. However so far the Higgs particle has not been seen and the field is open for discoveries at LHC. While the standard model is a kind of minimal model there are many other models within the branch of supersymmetric theories which predict a forest of new particles within the range of LHC.

As will be seen later, particles decaying to electrons will be one of the main entry points to all new physics. Hence electron identification will be one of the important points for a detector at LHC. It is also the scope for the work presented here, which combines analysis of a testmodule for electron identification and tracking at the ATLAS detector with simulations done

for expected physics at LHC energies, where electron identification will be important.

The work is based partly on independent research and partly on research done by other people within the ATLAS experiment. The aim has been to provide a reference report for all the areas of physics at LHC where electron identification will be important. Even though by references it should be clear where I summarise from others work, I will here give a short list of the chapters and sections based on my own work.

- Chapter 4 on analysis of testbeam data.
- The development of software to identify conversion described in section 5.7.
- In the chapter on the physics potential of electron identification the sections 6.2 and 6.4 on the $H \rightarrow \gamma\gamma$ decay and calibration of the calorimeter.
- The sections 6.3 and 6.5 on electron identification and b-tagging are partly done by me.

The remaining sections in the chapter on the physics potential are mostly based on external references.

I would like to thank many people who have helped me with this work. First of all my supervisor in Lund Torsten Åkesson as well as John Renner Hansen from NBI, Copenhagen. The complete TRT group for the ATLAS detector has been a great help both during the practical work at the testbeam during the summer 1995 and for the long analysis of the data afterwards. I would also like to thank the Swedish Research Council for paying my PhD studies at Lund University and the Danish Research Academy for supporting my stay in Sweden.

Chapter 2

Design of the ATLAS detector

2.1 Overall Design

With the presentation of the ATLAS Technical Proposal [1] in December 1994 and the approval of the ATLAS detector by the CERN research board in the start of 1996 the ATLAS detector has already taken a major step towards doing particle physics. The commission of the detector still lies 8 years ahead but the design of all major parts and most details are already frozen. The very long production time of the different detector parts makes this necessary.

As seen in fig. 2.1 the design of ATLAS looks like todays LEP detectors but major differences hide in the figure. The detector is much larger and has in addition to the solenoidal magnetic field in the inner detector a toroidal field in the outer muon detector. The coordinate system is defined in fig. 2.2.

The very large muon system consists of drift chambers positioned in three layers covering both the central parts and the endcaps of the detector. The toroidal field in the muon detector makes it possible to have an independent measurement of both position and momentum in the muon detector system.

The calorimeter is built up of several layers. From the inside out first the presampler is seen followed by a liquid argon calorimeter and outermost a hadron calorimeter using scintillators as active detector elements.

The inner detector, ID, utilises 2 different technologies. Closest to the interacting region are precision silicon detectors, placed in cylinders in the central rapidity region, the ID barrel, and in wheels in the high rapidity regions, the ID endcaps. Outside this is the Transition Radiation Tracker, TRT, which is a combined electron identification device and a tracker. It consists of thin proportional chambers in the form of straws, either embedded in fibres or with foils and straws in layers.

atlas.epsi

Figure 2.1: The design of the ATLAS detector. The detector is 42 m long and has a radius of 11 m.

The environment for a detector at LHC is very tough. Every 25 ns bunches will collide in the detector giving rise to 23 inelastic proton-proton collisions on the average at the design luminosity $L = 10^{34}\,\mathrm{cm}^{-2}\mathrm{s}^{-1}$. Events can only be written to tape at a frequency of 10-100 Hz which sets great demands on the trigger system to reduce the rate from the initial 40 MHz. For the first three years of data taking, LHC will run with an initial luminosity a factor 10 below the design luminosity. Those years will be very important for especially B-physics with the fewer collisions in each bunch crossing. 'The notation low luminosity refers to this initial luminosity of $L = 10^{33}\,\mathrm{cm}^{-2}\mathrm{s}^{-1}$.

The theoretical expectations for the physics events at pp collisions with $E_{\mathrm{CMS}} = 14\,\mathrm{TeV}$ are an enormous amount of events containing hadrons from QCD scattering and nothing else. The hard scattering events containing new physics will be at a much lower rate as indicated in fig. 2.3. The sign for creation of Higgs, heavy vector bosons, gluinos, and heavy quarks (t,b) are in most cases one or more high p_{T} leptons. Simultaneously there will be initial and final state radiation from the hard scattering event itself and

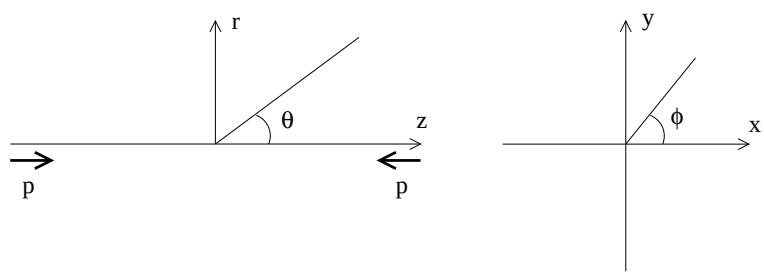

Figure 2.2: The coordinate system for the ATLAS detector. The directions of the two proton beams are shown. The radial coordinate r is defined as $r = \sqrt{x^2 + y^2}$ and the pseudorapidity η defined as $\eta = -\log \tan \frac{\theta}{2}$.

QCD background from the other events in the same bunch crossing.

With those considerations one can ask if a detector only having a precision muon detection and nothing else would be sufficient as a detector at LHC. Of the main interesting events a sole muon system would be able to detect

- Higgs decay into $\mathrm{ZZ(ZZ^*)} \rightarrow \mu^+\mu^-\mu^+\mu^-$.
- Like sign muon decays from production of gluino pairs.
- Semi-leptonic decays of top quarks.

By including a calorimeter system inside the muon detector the list is extended by

- The same items as above but with decay into electrons. For the Higgs this means a 4 times larger signal since also the mixed channel $\mathrm{H} \rightarrow \mathrm{ZZ(ZZ^*)} \rightarrow \mu^+\mu^-\mathrm{e}^+\mathrm{e}^-$ becomes accessible.
- In the case of a Higgs boson mass below 100 GeV where the 4 lepton channel has an extremely low cross section, the $\mathrm{H} \rightarrow \gamma\gamma$ channel becomes accessible but with very high requirements on the calorimeter.
- Supersymmetric theories can be tested since these often involve decays into the lightest supersymmetric particle which escapes detection. Large missing transverse momenta in connection with high energy jets will be a signature.

What is stated above is not entirely true since the rate of high p_T electrons to jets will be around 10^{-5} and a calorimeter system will not be able to reject these jets to an acceptable level. A further discussion of this can be found in section 6.3. For a sufficient rejection an inner tracking detector is required which also opens up a few more physics channels

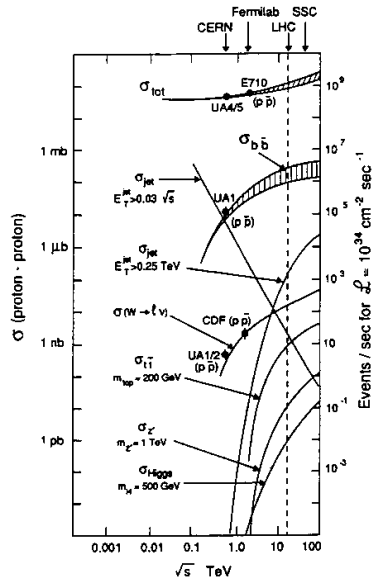

Figure 2.3: Expected cross section versus energy in the centre of mass system for pp collisions. Note the difference between the total inelastic cross section and the cross section for physics processes like Higgs production. From [2].

- CP-violation in the B-system. This involves reconstruction of J/Ψ and K_s^0. Also rare or forbidden decays in the Standard Model like $B \rightarrow \mu^+\mu^-$ may be studied.
- B-tagging for identification of $H \rightarrow b\bar{b}$ and top physics.
- Decay of a supersymmetric pseudoscalar $A \rightarrow \tau^+\tau^-$.

It is clear from the above that a true multi purpose detector at LHC needs to have all three main detector parts. This also gives the best assurance to discover new and totally unexpected physics.

2.2 The muon system

The detection of muons is done inside the huge toroidal magnetic field. A toroidal magnetic configuration has the advantage that the field integral $\int Bldl$, which determines the momentum resolution can be kept high even into very forward parts of the detector.

An air-core solution as seen in fig. 2.4 has been chosen to keep the stopping of muons within the system as low as possible, and also allow measurements

points inside the magnetic field. The minimum muon p_T detectable is around 3 GeV/c and limited by the stopping of low energy muons in the hadron calorimeter.

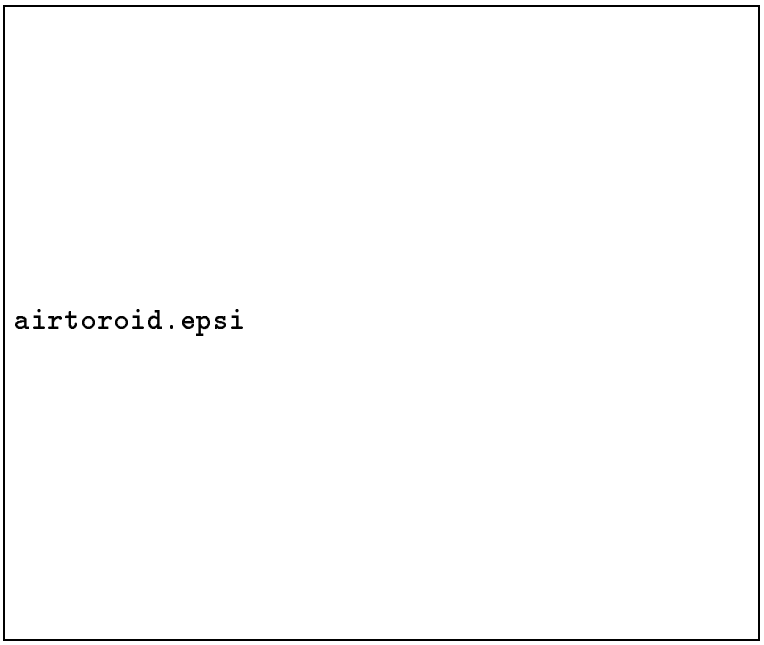

Figure 2.4: The aircore magnet with the toroidal field. In the present design of the ATLAS detector the number of coils have been changed from 12, as in the figure, to 8.

The momenta and position of the tracks are measured by 3 superlayers where the inner and outer one gives the position and the one in the middle provides the sagitta for the momentum measurement. Sagitta is the distance from a straight line joining the 2 endpoints of the track to a point on the track in between. It measures the curvature of the track and thereby the momenta.

To keep the fake track rate low and help the pattern recognition each superlayer consist of three layers and will in this way provide vectors that may be extrapolated into the other superlayers.

Since the precision chambers are far too slow for the trigger system there will be a separate set of trigger cells. The 2 main demands from physics on the level 1 trigger system are

- At low luminosity the low p_T threshold has to be as low as possible for the B-physics where a muonic decay of a B-meson is used as level 1 trigger. The present design sets the limit at $p_T = 6$ GeV/c.

- At high luminosity a sharp p_T threshold is very important. Events that are lost at the trigger level will never be recovered so the selection has to be as well defined as possible. Also the trigger rate is highly affected by a sharp threshold due to the rapidly falling p_T spectrum of the muons.

2.3 The calorimeter

The electromagnetic part of the ATLAS calorimeter is a liquid argon calorimeter with plates of lead placed as absorbers inside liquid argon. It works as a sampling calorimeter with the shower developing in the lead and the ionisation detected in the argon. The electromagnetic calorimeter is segmented into squares of $\Delta\eta \times \Delta\varphi = 0.025 \times 0.025$. However to be able to separate the 2 photons from π^0 decay the first layer of the calorimeter has a finer segmentation in η of 0.003. Since the photons can converge and the electrons bend in φ due to the magnetic field there would only be a limited gain by also having finer granulation in the φ direction as well.

Since the angular resolution for photons in the calorimeter is not good enough for the strict requirements for the $H \rightarrow \gamma\gamma$ decay a presampler is added to the design in the barrel region. The presampler is a thin calorimeter placed just behind the cryostat wall. As well as the first layer in the real calorimeter it has a fine grained resolution in η and together with the distance between the presampler and the calorimeter of 6 cm, an angular resolution of

$$\sigma(\theta) = \frac{40 \text{ mrad}}{\sqrt{E(\text{GeV})}} \tag{2.1}$$

is possible.

The calorimeter is required to detect signals with a very large dynamic range. At the lowest energies are detection of semileptonic decays of B-mesons with energies down below 1 GeV and the highest point of the scale is given by the discovery limit of excited Z or W states at around 5 TeV. In a decay like $Z' \rightarrow e^+e^-$ the electrons can reach energies as high as 3 TeV. The resolution at the energies below 20 GeV are limited by noise while the resolution in the high energy range is limited by a constant term from an inaccurate energy scale. The goal for the electromagnetic calorimeter is to reach a resolution

$$\frac{\sigma(E)}{E} = 0.01 \oplus \frac{0.10}{\sqrt{E}} \oplus \frac{0.40}{E} \tag{2.2}$$

where the first term is the constant term, the second the usual sampling term for calorimeters and the third is due to the noise in the electronics. All

energies are measured in GeV.

The main purpose of the hadron calorimeters in ATLAS will be to identify jets and to measure total missing transverse energy. For identification of isolated electrons it is also very important to measure the energy deposited behind the electromagnetic calorimeter. The measurement of missing energy requires to detect energy deposited in all directions. Hence the hadron calorimeter will reach down to $|\eta| = 5$ or almost 2 units of rapidity further than the electromagnetic calorimeter. In the barrel region the cheapest technology of iron absorbers with scintillator plates in between is adopted. The limited radiation hardness of the scintillators prevents them from being used in the forward region where a liquid argon calorimeter, as for the electromagnetic calorimeter, is in the design.

The granularity of individual detection elements will in the barrel region be $\Delta\eta \times \Delta\varphi = 0.1 \times 0.1$ and in the forward region $\Delta\eta \times \Delta\varphi = 0.2 \times 0.2$. Intrinsic effects in the hadronic shower development limits the theoretical obtainable resolution to similar numbers.

The thickness of the hadron calorimeter is limited by several factors. A thick calorimeter will increase the size and price of the surrounding muon system and at the same time increase the interaction with muons. On the other hand a thinner calorimeter increases the punch through of hadrons to the muon system where they will be identified as muons. For ATLAS a total thickness of the calorimeter of 11 absorption lengths has been chosen. This gives almost as many hadrons as muons in the muon system leading to an increased rate for the muon system and the trigger system in general since the trigger is very dependent on muon identification.

2.4 The inner detector

To ensure the optimal calorimeter performance there are very hard constraints on the amount of material in the inner detector. For electrons material causes bremsstrahlung which degrades the energy resolution and for photons conversions in the material makes the identification task harder.

Also in volume, the ID is limited from all sides. To keep the cost of the complete detector down the outer radius and length of the ID are limited to $r = 110$ cm and $|z| = 340$ cm. The inner radius is determined by radiation damage. For 10 years of operation at LHC it is currently believed that the minimum radius for a silicon strip detector to ensure survival is around 20 cm. Two very different technologies have been accepted for the inner detector.

2.4.1 Precision tracking

To give the best performance on vertex reconstruction and momentum resolution, a tracker of semiconducting silicon layers is placed in the innermost volume of the inner detector. This is again divided into several parts with pixel detectors as the 2 innermost passed layers and strip detectors outside. With a minimum of 6 passed layers for all $|\eta| \leq 2.2$ a resolution of $\frac{\sigma(p)}{p} = 6 \cdot 10^{-4} p\,(\mathrm{GeV})$ in momentum and an impact parameter resolution around $\sigma = 30\ \mu$m will be obtainable. In the latest design the silicon layers are spread out as evenly as possible along the track to ensure a mimimal correlation between background hits and thereby strengthen the pattern recognition.

2.4.2 Transition radiation tracker

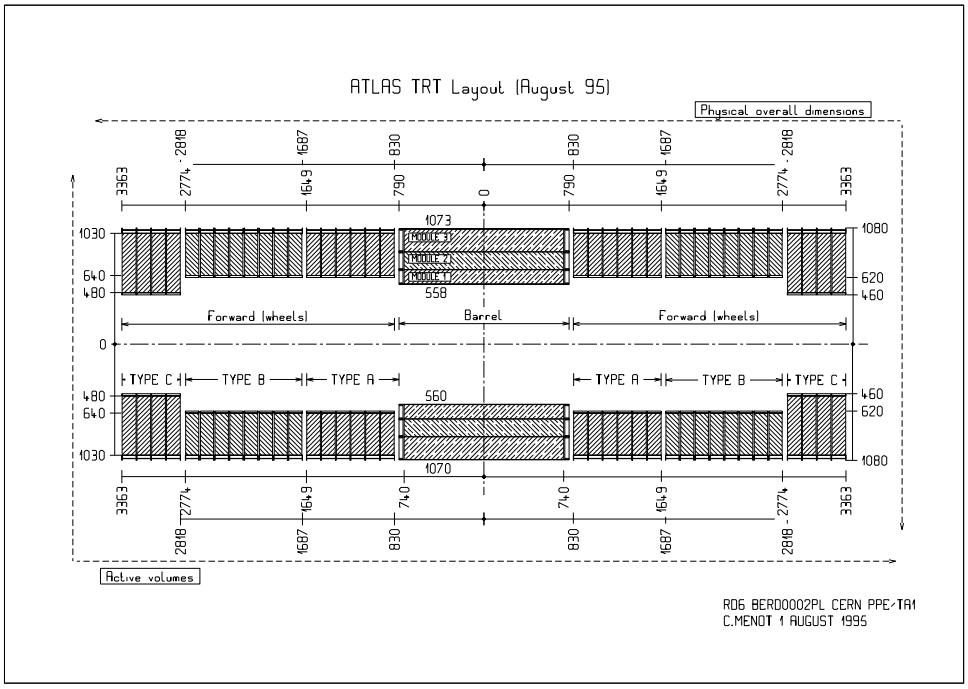

Figure 2.5: The design of the Transition Radiation Tracker in ATLAS.The central part of the TRT, the Barrel TRT, is a modular structure with 32 modules in each of the 3 cylinders. The Endcap TRT at high rapidities has the straws placed radially in wheels. The silicon tracker is placed in layers and wheels inside the TRT.

The outer part of the tracker will be filled with the Transition Radiation Tracker. In this section the general layout will be described while the theory behind transition radiation will be treated separately in chapter 3. The general design of the TRT can be seen in fig. 2.5. The TRT consists of thin proportional chambers either in the form of straws embedded in fibres or with foils and straws in separate layers.

In total there are around 370000 4 mm straws in the TRT, which are placed radially in the endcap and longitudinally in the barrel region. These orientations are chosen to maximise the number of straws passed for all directions pointing away from the interaction point. In the endcap the straws are placed in wheels where layers of radiator foils and layers of straws are interspaced.

A more complicated structure is required in the barrel where the lack of space prevents a solution with straws and radiator in separate layers. Instead the radiator will be put into all available space around the straws as fibre sheets.

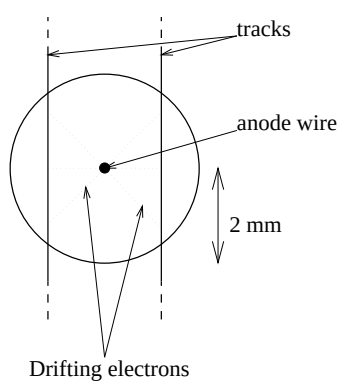

Figure 2.6: In a single straw the drift time will tell the distance from the anode wire where the track passed but not on which side. This ambiguity problem is solved by considering several rows of straws shifted with respect to each other.

Each straw acts as a proportional chamber. A charged particle crossing the straw creates an electron cloud that drifts to the anode wire where it is amplified and detected. From the drift time the point of passage can be determined with a 2 fold ambiguity as shown in fig. 2.6. This ambiguity will be solved using the correlation with the other passed straws at the reconstruction stage.

The readout electronics from the straws are designed to measure 2 thresholds for the energy deposited on the anode wire. The lower one at 200 eV will

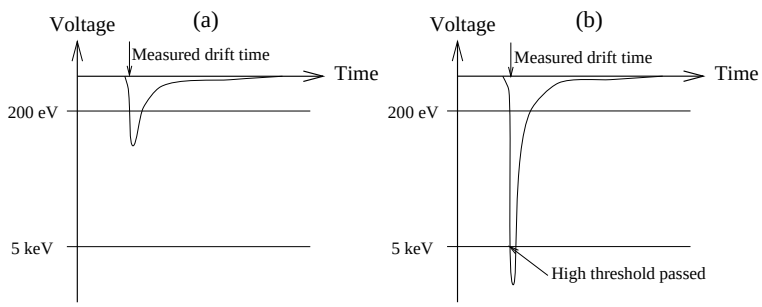

Figure 2.7: A sketch of the voltage read out from the straw in the case of a minimum ionising particle (a) and the same situation with detection of both a minimum ionising particle and X-rays from transition radiation (b).

detect minimum ionising particles while the higher threshold at 5-7 keV will detect X-rays from transition radiation as seen in fig. 2.7. To allow a high absorption for X-rays the straws have a Xe gas mixture ($70\%Xe, 10\%CO_2, 20\%CF_4$). While this gives high efficiency for detection of X-rays the high Z Xe-component deteriorates the track resolution to a single straw resolution of around $150\mu m$.

A summary of the parameters for the TRT is given in table 2.1.

straw	radius length	2 mm 160 cm (barrel) 40 cm (endcap)
wire	diameter material	30 μm Gold on Tungsten
gas	pressure temperature mix	1 atm $15 \pm 5°C$ 70% Xe 20% CF_4 10% CO_2
fibre	material density thickness	PE/PP 0.06 gcm^{-3} 15 μm
foils	material thickness	PE/PP 15 μm

Table 2.1: A summary of the parameters of the TRT.

Chapter 3

Transition radiation

Transition radiation is a radiation in the X-ray region, that arises when ultrarelativistic particles cross a boundary between 2 media with different dielectric constant. It depends strongly on the relativistic γ factor of the particle which makes it usable for particle identification at energies where time of flight methods or detection of Čerenkov radiation no longer work. As an example, the large mass difference between electrons and pions makes it possible to do electron pion separation in an energy interval from 0.5 GeV to 200 GeV.

To build a detector based on transition radiation is far from easy though since the number of X-ray photons from a single boundary are of the order of the fine structure constant α.

The theory here is mainly based on the review articles [3] and [4] and the section on applications to detectors on [5] and [6].

3.1 Transition radiation from a single boundary

The simplest situation creating transition radiation is with only one boundary as indicated in fig. 3.1. In both media there is a solution to the inhomogenous Maxwell equations including the particle. Since this is a particle moving in a straight line inside a homogeneous medium there is no radiation. However to fulfil the boundary conditions on the surface between the two media it is necessary to add solutions to the homogenous Maxwell equations. This homogenous solution is the transition radiation.

For the electric field at the boundary, in the limit of ultrarelativistic

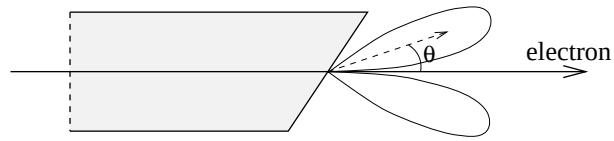

Figure 3.1: Transition radiation created at a single boundary between 2 media. θ is highly exaggerated on the figure.

particles, the electric field is apart from some numeric constants

$$\vec{e}(\omega,\vec{\theta}) = \frac{\vec{\theta}}{\gamma^{-2}+\theta^2+\xi_1^2} - \frac{\vec{\theta}}{\gamma^{-2}+\theta^2+\xi_2^2}. \tag{3.1}$$

with a similar formula for the magnetic field $\vec{h}(\omega,\vec{\theta})$. $\vec{\theta}$ is the difference between the unit vectors in the direction of the particle and the photon. γ is the relativistic gamma factor of the particle and

$$\xi_i = \frac{\omega_{\mathrm{P}_i}}{\omega}. \tag{3.2}$$

ω_{P_i} is the plasma frequency of a material i with electron density n_{e_i} considered as an electron gas,

$$\omega_{\mathrm{P}_i} = \frac{4\pi\alpha n_{\mathrm{e}_i}}{m_{\mathrm{e}}}. \tag{3.3}$$

The definition of θ can be seen in fig. 3.1.

The energy radiated per solid angle per unit frequency takes the form

$$\begin{aligned}\frac{\mathrm{d}^2W}{\mathrm{d}\omega\mathrm{d}\Omega} &= \left|\vec{e}(\omega,\vec{\theta})\times\vec{h}(\omega,\vec{\theta})\right| \\ &= \frac{\alpha}{\pi^2}\left|\frac{\theta}{\gamma^{-2}+\theta^2+\xi_1^2} - \frac{\theta}{\gamma^{-2}+\theta^2+\xi_2^2}\right|^2 .\end{aligned} \tag{3.4}$$

The angular distribution is illustrated in fig. 3.2.

Performing the angular integration in (3.4) the total energy radiated per unit frequency is

$$\frac{\mathrm{d}W}{\mathrm{d}\omega} = \frac{\alpha}{\pi}\left(\frac{\xi_1^2+\xi_2^2+2\gamma^{-2}}{\xi_1^2-\xi_2^2}\log\frac{\gamma^{-2}+\xi_1^2}{\gamma^{-2}+\xi_2^2} - 2\right) \tag{3.5}$$

or after a further integration over frequency

$$W = \frac{2\alpha\gamma\omega_{\mathrm{P}_1}}{3} \tag{3.6}$$

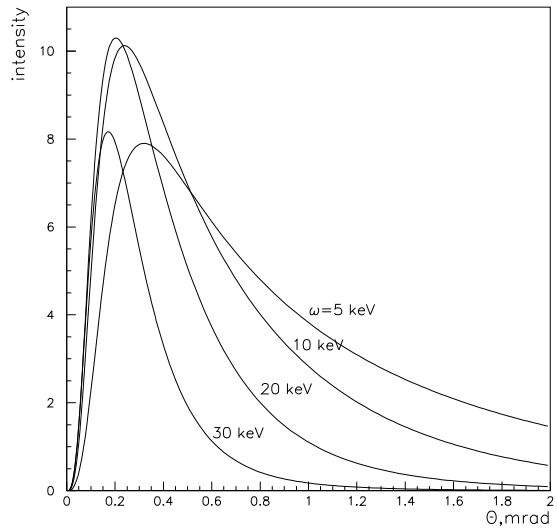

Figure 3.2: The angular distribution $\frac{d^2W}{d\omega d\theta}$ of transition radiation from a single boundary between polypropylene and air for a 4 GeV electron ($\gamma = 8000$).

under the assumption $\omega_{P_2} \ll \omega_{P_1}$.

In the ideal situation here the transition radiation is proportional to γ but the proportionality cannot be preserved in a practical detector.

Taking into account a low energy cut-off which will exist in all detectors the number of photons emitted from a single boundary is

$$n_\gamma = \int_{\omega_{\min}}^{\infty} \frac{1}{\omega} \frac{dW}{d\omega} d\omega \simeq 0.5\alpha \tag{3.7}$$

with $\omega_{\min} = 0.15\gamma\omega_P$ as an example. Here lies the main problem for detectors based on transition radiation. The number of emitted photons from a single surface is very low, and hence many surfaces are needed. However many closely packed surfaces also offer the possibility to use interference in a threshold detector.

3.2 Radiators with many layers

A detector with many boundaries can be achieved using foils placed closely together as shown in fig. 3.3. Simply a stack of foils is called a radiator.

With one boundary two different stationary solutions to the Maxwell equations had to be matched, but with many boundaries a general solution

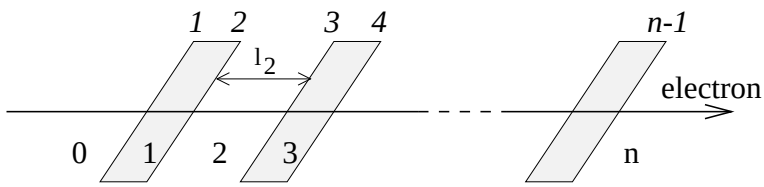

Figure 3.3: A radiator with many boundaries. The media are numbered from 1 to n and the boundaries in *italics* from 1 to $n-1$.

would be very complicated. But as seen in (3.4) and fig. 3.2 the radiation is sharply peaked in the forward direction and from (3.5) with frequencies in the X-ray region. Hence backwards radiation and reflections can be ignored. With this simplification the electric field at the end of the radiator is given by adding up the field from the individual boundaries taking interference and absorption into account.

$$\vec{E}(\omega,\vec{\theta}) = \sum_{j=1}^{n-1} \vec{e}^{j}(\omega,\vec{\theta}) \exp\left(-\sum_{\mathrm{m}\geq \mathrm{j}}^{\mathrm{n}-1} \sigma_{\mathrm{m}} + i\varphi_{\mathrm{m}}\right). \tag{3.8}$$

$\vec{e}^{j}$ is the single surface amplitude as in (3.1) with the media surrounding boundary j substituting ξ_1 and ξ_2. σ_m is the absorption coefficient for layer m and φ_m the difference in phase for transition radiation from different layers caused by different times for the particle and the photons to cross the layers.

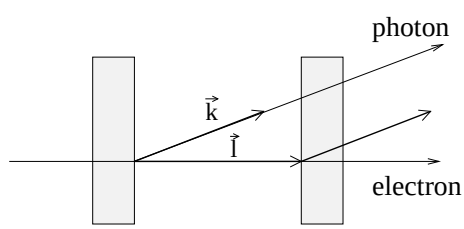

Figure 3.4: The phase difference of transition radiation from different boundaries is affected by the wave vector in the media, the velocity of the particle and the distance between the boundaries.

$$\varphi_{\mathrm{m}} = \frac{\omega l_{\mathrm{m}}}{v} - \vec{k}_{\mathrm{m}} \cdot \vec{l}_{\mathrm{m}} \tag{3.9}$$

where v is the velocity of the particle, $\vec{k}_{\mathrm{m}}$ the wave vector of the photon with frequency ω and $\vec{l}_{\mathrm{m}}$ the vector between the crossing points of the boundaries and the particle as illustrated in fig. 3.4.

The phase difference can be simplified using

$$\epsilon_{\mathrm{m}} = 1 - \xi_{\mathrm{m}}^2 \tag{3.10}$$

$$k_{\mathrm{m}} = \sqrt{\epsilon_{\mathrm{m}}}\omega \simeq \left(1 - \frac{1}{2}\xi_{\mathrm{m}}^2\right) \tag{3.11}$$

$$\frac{1}{v} \simeq 1 + \frac{\gamma^{-2}}{2} \tag{3.12}$$

$$\vec{k}_{\mathrm{m}} \cdot \vec{l}_{\mathrm{m}} = k_{\mathrm{m}} l_{\mathrm{m}} \cos\theta \simeq k_{\mathrm{m}} l_{\mathrm{m}} \left(1 - \frac{1}{2}\theta^2\right) \tag{3.13}$$

resulting in

$$\varphi_{\mathrm{m}} = \frac{(\gamma^{-2} + \theta^2 + \xi_{\mathrm{m}}^2)\omega l_{\mathrm{m}}}{2}. \tag{3.14}$$

Defining the formation length

$$z_{\mathrm{m}} = \frac{2}{(\gamma^{-2} + \theta^2 + \xi_{\mathrm{m}}^2)\omega} \tag{3.15}$$

it is seen that with $l_{\mathrm{m}} \ll z_{\mathrm{m}}$ the 2 boundaries of the m'th media will have negative interference and there will be no transition radiation. The interpretation is that creation of transition radiation is in fact a macroscopic effect, called the formation zone effect, requiring a certain thickness of each layer in the radiator.

For a single foil placed in a gas with no absorption

$$\left(\frac{\mathrm{d}^2 W}{\mathrm{d}\omega \mathrm{d}\Omega}\right)_{1\mathrm{foil}} = \left(\frac{\mathrm{d}^2 W}{\mathrm{d}\omega \mathrm{d}\Omega}\right)_{1\mathrm{boundary}} 4\sin^2(\varphi/2) \tag{3.16}$$

using (3.1), (3.4) and (3.8). Since the interference is included in the angular integration of the radiated energy it turns into a very complicated integral. It is normally expressed in terms of the dimensionless variables ν and Γ

$$\nu = \frac{2\omega}{l_1 \omega_{\mathrm{P}_1}^2} \tag{3.17}$$

$$\Gamma = \frac{2\gamma}{l_1 \omega_{\mathrm{P}_1}}. \tag{3.18}$$

ν and Γ are defined such that $\nu, \Gamma > 1$ is the region where there is no transition radiation due to the formation zone effect.

For a single foil placed in vacuum

$$\left(\frac{\mathrm{d}W}{\mathrm{d}\omega}\right)_{1\mathrm{foil}}^{\mathrm{vacuum}} = \frac{2\alpha}{\pi} G(\nu, \Gamma) \tag{3.19}$$

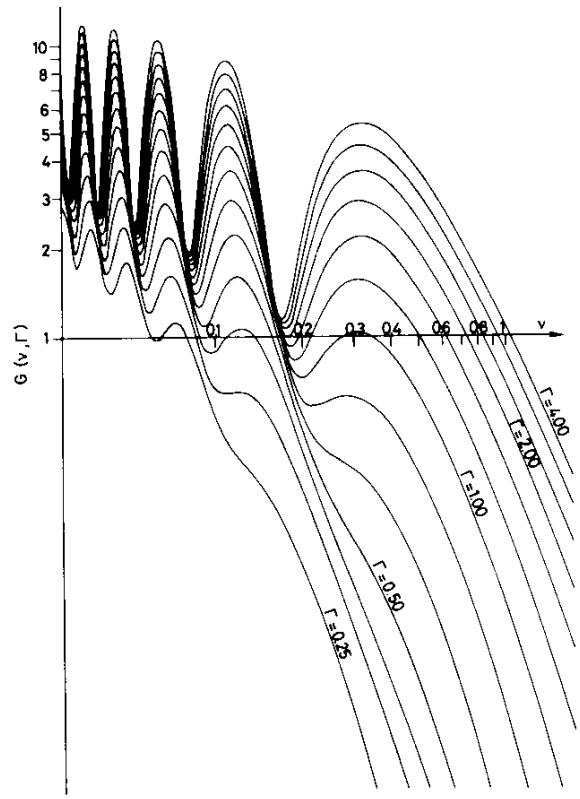

Figure 3.5: The transition radiation yield from a single foil expressed through the universal function $G(\nu, \Gamma)$. Note the broad maximum around $\nu = 1/\pi$. From [3].

with $G(\nu, \Gamma)$ plotted in fig. 3.5. The broad maximum around $\nu = 1/\pi$ is important for the design of a detector as described in section 3.5. The equation (3.19) only apply to the case with vacuum outside the foils, $\omega_{P_2} = 0$, but can be extended to the non-vacuum introducing ω'_{P_i} and γ'

$$\omega'_{P_1} = (\omega^2_{P_1} - \omega^2_{P_2})^{1/2} \tag{3.20}$$

$$\omega'_{P_2} = 0 \tag{3.21}$$

$$\gamma' = (\gamma^{-2} + \omega^2_{P_2}/\omega^2)^{-1/2}. \tag{3.22}$$

In (3.1), (3.4) and (3.8) γ^{-2} and ξ_i^2 enters only in the combination $\gamma^{-2} + \xi_i^2$ which is preserved when substituting ω_{P_i} and γ by ω'_{P_i} and γ'. The substitution transforms the general case into the case with vacuum between the foils

and (3.19) can be used.

$$\left(\frac{\mathrm{d}W}{\mathrm{d}\omega}\right)_{1\mathrm{foil}} = \frac{2\alpha}{\pi} G(\nu', \Gamma') \tag{3.23}$$

where ν' and Γ' are defined using ω'_{P_1} and γ' in (3.17) and (3.18).

From (3.20) it is seen that $\omega'_{\mathrm{P}_1} < \omega_{\mathrm{P}_1}$ and $\gamma' < \gamma$ resulting in a lower yield from a detector with gas instead of vacuum between the foils. Also the nice feature of a linear response to γ as seen in (3.6) disappears. Instead there is a saturation in the transition radiation at

$$\gamma \geq \gamma'(\gamma = \infty) = \frac{\omega}{\omega_{\mathrm{P}_2}}. \tag{3.24}$$

3.3 N foils placed with regular spacing

In analogy to (3.16) the radiated energy from a radiator with N equal foils with regular spacing is

$$\left(\frac{\mathrm{d}^2W}{\mathrm{d}\omega\mathrm{d}\Omega}\right)_{\mathrm{Nfoils}} = \left(\frac{\mathrm{d}^2W}{\mathrm{d}\omega\mathrm{d}\Omega}\right)_{1\mathrm{foil}} \left|\frac{1-C^{\mathrm{N}}}{1-C}\right|^2 \tag{3.25}$$

where

$$C = \exp\left(i\varphi_1 + i\varphi_2 - \frac{1}{2}\sigma_1 - \frac{1}{2}\sigma_2\right). \tag{3.26}$$

The mean value of the interference factor in (3.25) shows how much is gained from having several foils. It can be defined as an effective number of foils

$$\mathrm{N}_{\mathrm{eff}} = \frac{1 - e^{-\mathrm{N}(\sigma_1+\sigma_2)}}{1 - e^{-(\sigma_1+\sigma_2)}}. \tag{3.27}$$

For $\mathrm{N}\sigma \ll 1$ the yield is proportional to N while for $\mathrm{N} > 1/\sigma$ there is as much X-rays absorbed as new are generated resulting in a saturation with $\mathrm{N}_{\mathrm{eff}} = 1/\sigma$.

It is from (3.25) and (3.26) clear that there will be a very dense interference pattern with resonances at emission angles θ where

$$\varphi_1 + \varphi_2 = 2p\pi,\ p \text{ integer} \tag{3.28}$$

or

$$\frac{(\gamma^{-2} + \theta^2 + \xi_1^2)\omega l_1}{2} + \frac{(\gamma^{-2} + \theta^2 + \xi_2^2)\omega l_2}{2} = 2p\pi,\ p \text{ integer} \tag{3.29}$$

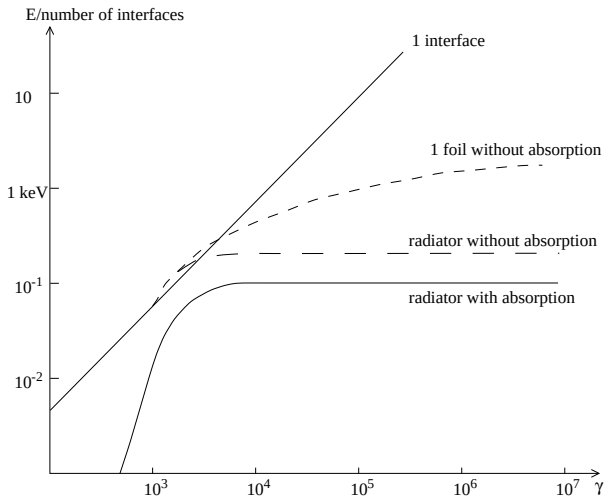

Figure 3.6: Energy radiated from a radiator with N foils compared to a single interface or 1 foil. The radiator has 400 layers of 20μm polypropylene with gaps of 180μm helium. It can clearly be seen how a detector with a multifoil radiator can act as a threshold detector. From [4] with minor corrections.

from (3.14). However it is not possible to measure the angular distribution and after the integration of emission angles θ the distribution is very similar to (3.23) as plotted in fig. 3.5 just scaled by N_{eff}. In fig. 3.6 is a plot of the energy from a radiator with regular spaced foils compared to the situation with a single interface or one foil. From the figure it is very clear how a detector with a multifoil radiator can be used as a threshold detector for particle identification. Electrons exceeds a γ factor of 1000 at energies of 0.5 GeV while pions first pass this limit at 140 GeV. Hence in the very large energy interval from 0.5 GeV to 140 GeV electrons will create full transition radiation while there will be practically no radiation from pions.

Radiators can be made of foam or fibres instead of regular foils. The irregularities in the thickness and spacing of the boundaries will cause a lower performance per unit length compared to regular foils. However for practical solutions foam and fibres can have advantages in terms of larger flexibility in the fabrication and placement of the radiator.

3.4 Detection of X-rays

The emission of X-rays from the radiator has to be matched to the absorption method used for the detection. If the ionisation of a gas is used for detection,

the frequency response is rather limited with a high Z gas like Xe as the best. The absorption length scales approximately like ω^3, in the range below 1 MeV where the photoelectric effect is dominant. Hence it is impossible for a practical gaseous detector to detect X-rays above 20 keV.

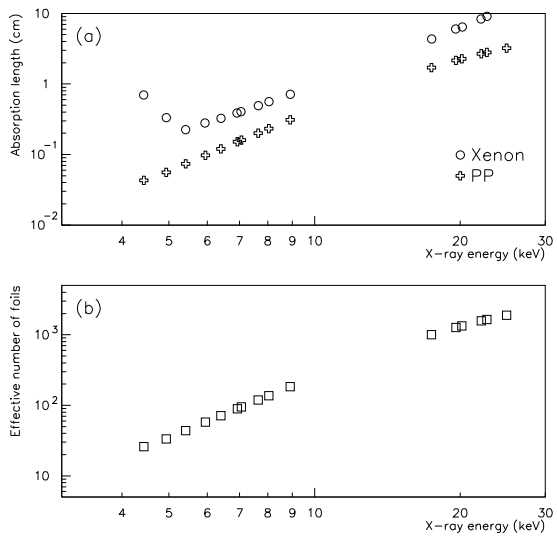

Figure 3.7: In (a) the absorption length of X-rays for xenon and polypropylene. In (b) is seen how the absorption length for PP can be expressed as a saturation value for the effective number of foils as described in section 3.3.

There is also a lower energy cutoff given by absorption. At energies below a few keV there will be too large absorption in the radiators and the walls surrounding the detecting gas. Both effects can be seen in fig. 3.7.

The foil thickness l_1 in a N-foil radiator can now be adjusted to make the maximal output correspond to the optimal frequency ω_{gas} for detection. In fig. 3.5 it is seen that the maximal output is around $\nu = 1/\pi$. Using (3.17) and (3.20)

$$l_{1_{\text{optimal}}} = \frac{2\pi\omega_{\text{gas}}}{\omega'^{\,2}_{\text{P}_1}}. \tag{3.30}$$

3.5 How to design a detector

A practical transition radiation detector will need to take into account all the physics from the preceding sections. In most cases the length of the

detector, L_{det}, is fixed either as a length along the beamline in a fixed target experiment or as radial space in a colliding beam detector.

With a fixed length of the detector, optimisation is required for.

- The foil thickness l_1, to get the correct wavelength distribution of the transition radiation.
- The distance between the foils l_2, which need to be large enough to avoid formation zone effects as derived in (3.15).
- The number of foils $\mathrm{N_{foil}}$ in front of a detecting gas.
- The gas composition and the thickness of the gas l_{gas} .

The choice of xenon as the detecting gas is obvious from its very short absorption length as seen in fig. 3.7. With a gas thickness of around 0.5 cm there is large absorption up to 10 keV. In part (b) of fig. 3.7 is seen that X-rays below 4 keV are absorbed in the radiator. This sets $\omega_{\mathrm{gas}} \approx 6$ keV. For the foil material where low absorption is very important a low Z material is the best. Since lithium and beryllium are very reactive materials the best practical choices are carbohydrates like polyethene or polypropylene. With ω_{gas} and the foil material fixed the optimal foil thickness can be calculated from (3.30) to $l_{1_{\mathrm{optimal}}} = 17\ \mu$m.

To perform well for emission angles above $\theta > 0.2$ mrad and for X-rays above 4 keV, (3.15) gives a minimal spacing of the foils of $l_{2_{\mathrm{minimal}}} = 0.13$ mm with air as the medium between the foils. Also it is seen in fig. 3.7 that the effective number of foils stay below 30 for 4 keV X-rays. Hence not much is gained by having $\mathrm{N_{foil}} > 30$.

Adding up the different lengths gives

$$l_{\mathrm{det}} = \mathrm{N_{foil}}(l_1 + l_2) + l_{\mathrm{gas}} \approx 10 \text{ mm} \tag{3.31}$$

with only a small gain by increasing this length. At the same time the detector is very inefficient with an average number of photons

$$n_\gamma = 4 n_{\gamma_{\text{single boundary}}} \mathrm{N_{eff}} \approx 0.5. \tag{3.32}$$

Only every second electron passing the detector will emit just 1 single transition radiation photon! The factor 4 comes from the optimised thickness of the foil for positive interference.

The solution to the problem is to place multiple copies of the detector behind each other. This also opens up the possibility to combine the particle identification with tracking. Each part consisting of a radiator and a gas for detection of X-rays will for future reference be called a layer.

To measure the energy deposited as ionisation in the xenon gas there are 2 methods called the Q and the N method.

In the Q method one measures with ADC's or FADC's the total energy deposited in the gas which is a sum of the transition radiation in the radiator and $\frac{\mathrm{d}E}{\mathrm{d}x}$ from the particle which also passes through the detecting gas. The method is sensitive to background from the Landau tail of $\frac{\mathrm{d}E}{\mathrm{d}x}$. Since the Q method is mainly sensitive to the X-rays with the highest energies, the number of foils can be enlarged in each layer because the absorption of X-rays in the radiator is only important for the soft part of the spectrum as seen in fig. 3.7.

The N method instead counts the number of clusters in the gas. A cluster is the volume of the gas where the ionisation from the electron knocked out by the X-ray photon is deposited. It typically has a diameter of 1 mm. The method is not very sensitive to $\frac{\mathrm{d}E}{\mathrm{d}x}$ since the main part of the ionisation is spatially spread out. Instead background comes mainly from δ-electrons. δ-electrons are electrons kicked out of the atomic shells by the primary particle with an energy high enough to make ionisation themselves.

While the Q method would be very expensive to implement for a multilayered detector with separate ADC's for each layer the N-method can be incorporated here in a very elegant way. A threshold on the deposited energy in a single layer can give a simple yes/no answer if there was a cluster in a given layer. The probability for multiple clusters in a single layer is low and only few clusters will be lost by just having output for cluster or no cluster. With a fixed probability for a cluster in each layer, particles passing all the layers cause a binomial distribution in the number of yes type answers.

The N method has to distinguish between two different binomial distributions from pions and electrons respectively for particle identification. The distributions have very different mean and for binomial distributions there are no suffering from a long Landau tail as with the Q method.

Since the total length of the detector is fixed and the length of each layer given by (3.31) also the number of layers is fixed. However for the N method what counts is the mean number of clusters in all layers given by

$$\overline{n_{\text{cluster}}} = N p_{\text{layer}} \tag{3.33}$$

where N is the number of layers and p_{layer} the probability for a cluster in each layer. This can also be expressed in terms of the number of detected clusters per unit length

$$A_{\text{TR}} = \frac{\mathrm{d}N_{\text{clusters detected}}}{\mathrm{d}L}. \tag{3.34}$$

While the lower limit on l_2 is not very stringent the thickness of the Xe absorption layers are fixed and hence

$$N_{\text{layer}} = \frac{L_{\text{det}}}{\text{N}_{\text{foil}}(l_1 + l_2) + l_{\text{gas}}} \tag{3.35}$$

reaches a saturation when l_2 is reduced to the point where $\text{N}_{\text{foil}}(l_1 + l_2) = l_{\text{gas}}$. But this is already the case for $l_2 = 0.13$ mm and a maximal performance of $A_{\text{TR}} \approx 0.15$ clusters/cm may be reached [6].

As can be seen the different optimisations have led to a design which is very close to the design of the ATLAS TRT as described in section 2.4.2.

3.6 Results from earlier transition radiation detectors

Experiment	R806	E715	NA34	UA6	UA2	E769	NA31	NA24
Length (cm)	55	360	70	55	22	130	110	60
N layers	2	12	8	3	2	24	4	4
Radiator	Li	CH_2	CH_2	Li	CH_2	CH_2	CH_2	CH_2
Method	Q	N	N	Q	Q	N	Q	N
Efficiency π (%)	5	0.06	0.05	10	8	2	10	0.5
Efficiency e (%)	90	99	90	90	80	87	98.7	80

Table 3.1: Performance of detectors used for electron pion separation. The method refers to the Q and N method as described in section 3.5. The rejection is the efficiency for pions at the efficiency of electrons given in the row below. From [6] with slight changes of notation.

Transition radiation detectors have been implemented in many different experiments within high energy physics, mainly for electron pion separation but also for separation of pions and heavier hadrons. However the mass difference between pions and kaons is so small that only a limited rejection power can be achieved in the later case. A summary of specifications and performances of earlier detectors are given in table (3.1).

The HELIOS TRD (NA34) is the only transition radiation detector which has combined the tracking and the transition radiation detection in the same way as planned for the ATLAS TRT.

The HELIOS experiment was an experiment for studying lepton production in proton-nucleus collisions. To select the electrons in the busy environment of background hadrons a very large rejection power was needed. This

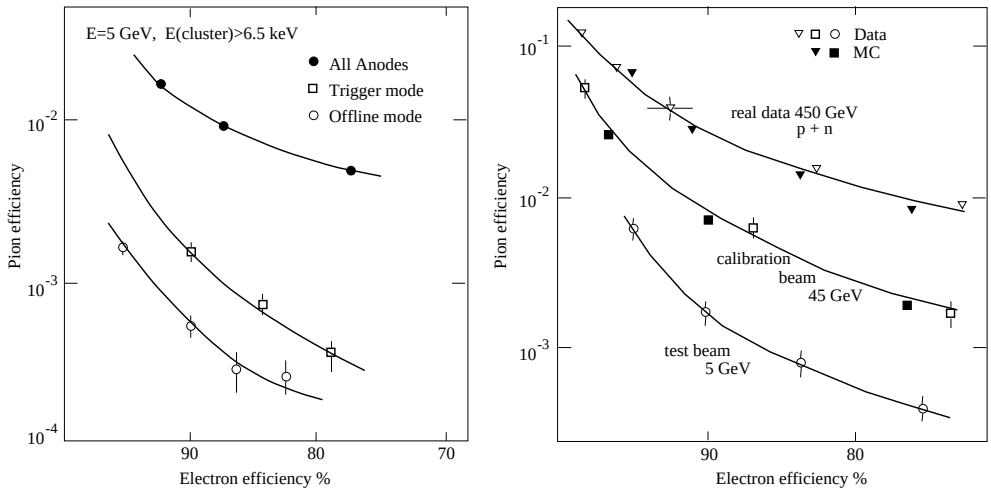

Figure 3.8: Performance of the HELIOS TRD. The first figure shows how the rejection power improves by including information on the position of the track. The information was first obtainable at the offline analysis. The second figure indicates the effect of having a high occupancy environment with many overlapping tracks in the proton-nucleus collisions. From [6].

was achieved with a combination of an uranium/liquid argon calorimeter and a transition radiation detector. The TRD had 8 layers each consisting of 200 foils of 12.7μm polypropylene and a multiwire proportional chamber filled with xenon for the X-ray detection. In this detector it proved very powerful to have the tracking together with the detection of transition radiation since this made it possible to sort out background from δ-electrons from other tracks as seen in fig. 3.8.

It was also in the HELIOS TRD proved that it is possible to operate a TRD with many overlapping tracks in the detector, however with a reduced rejection of pions. The effect was fully understood as indicated in the second part of fig. 3.8 where both data points and Monte Carlo simulations are plotted.

Chapter 4

The 95 test of the endcap prototype

4.1 Setup in the test beam

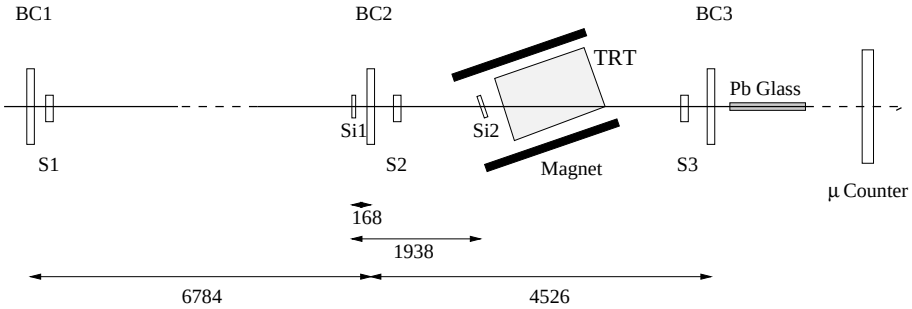

Figure 4.1: The setup for the TRT prototype in August 95. S1, S2 and S3 indicates scintillators, BC are beam chambers and Si1 and Si2 the crossed strip silicon detectors. The magnet is rotated 19.2 degrees around a vertical axis to give a magnetic field in the bending plane. All lengths are measured in mm.

During the summer of 1995 the endcap TRT prototype build by the RD6 collaboration was placed in the H8 testbeam in the North Hall at CERN. The prototype consist of 5 sections each having 16 layers of straws. The straws are 40 cm long and are placed with 1 degree intervals in a disk structure. The straws have an active radius from 31.5 cm to 66.5 cm. In front of each straw layer are 17 layers of 15μm polypropylene sheets acting as a radiator. The complete setup can be seen in fig. 4.1 with a closeup of the magnet and the TRT prototype in fig. 4.2.

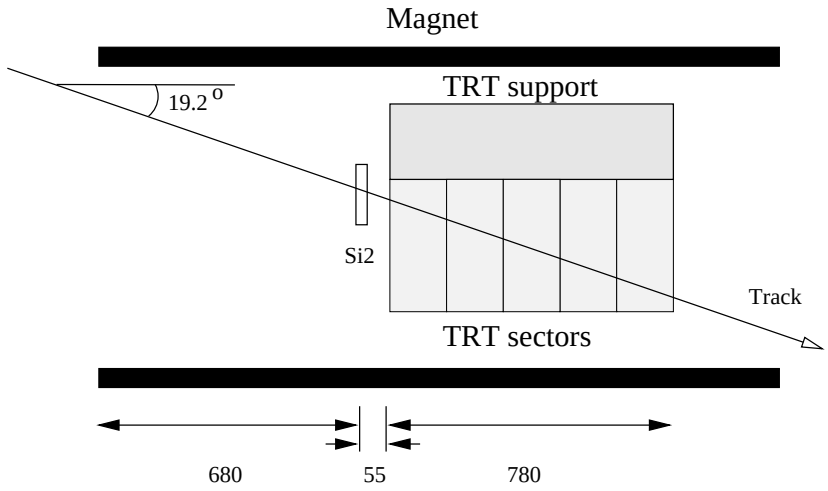

Figure 4.2: A close up of the magnet and the TRT prototype in the test beam. The 0.8 T solenoidal field gives a 0.257 T field in the bending plane.

For the tracking and particle identification tests the beam was either a 20 GeV secondary electron or pion beam from the CERN SPS. To test the TRT prototype it is essential to have both track position and particle identification provided externally. For the tracking this can be done with the three beam chambers BC1, BC2 and BC3 and two crossed strip silicon detectors Si1 and Si2. The resolution is approximate 400μm for the beam chambers, while the silicon strips have a pitch of 50μm with analog read out. Hence charge division can give a resolution better than the 16μm Gaussian resolution obtainable from a binary read out.

Particle identification is done with a Čerenkov counter, a multiplicity counter and a lead glass calorimeter. The multiplicity counter is a preshower consisting of a small amount of lead and a scintillator mounted directly in front of the calorimeter. Histograms of the response from the 20 GeV pion and electron beam can be seen in fig. 4.3 with the cuts for purification indicated.

Triggering is done by scintillators where S1 is only 1×0.5 cm^2 to ensure a narrow beam. The TRT prototype is placed inside a solenoidal magnet rotated 19.2° around a vertical axis. The solenoid can give a field of 0.8 T which gives an effective 0.257 T in the bending plane.

A simple event display program has been constructed for the testbeam. In fig. 4.4 are seen a single pion and a single electron in the detector. Both the tracking and the electron identification capability are clearly seen.

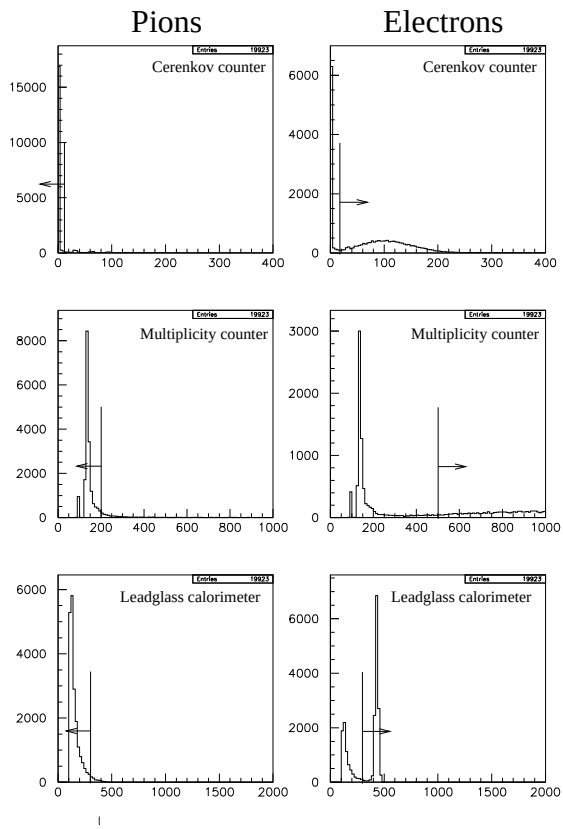

Figure 4.3: Histograms with the response of the Čerenkov counter, the multiplicity counter, and the lead glass calorimeter. The 2 beams are pions (left) and electrons (right). Also indicated on the graphs are the cuts to ensure a pure pion (electron) beam.

4.2 Frontend electronics for the prototype

The 95 setup is the first successful setup of a prototype fully equipped with LHC-like electronics. The purpose of the front end electronics is to translate the incoming analog pulses on the anode wires to a digital signal which can be transmitted to the data acquisition system. The incoming voltage will give information on when a particle passes the straw and if transition radiation was detected together with the normal $\frac{\mathrm{d}E}{\mathrm{d}x}$.

As can be seen in fig. 4.5 the anode wire signals run into the TRDA where they are shaped with a 12.5 ns rise time and tail cancellation. The latter is very important to keep the baseline from drifting considering the high count

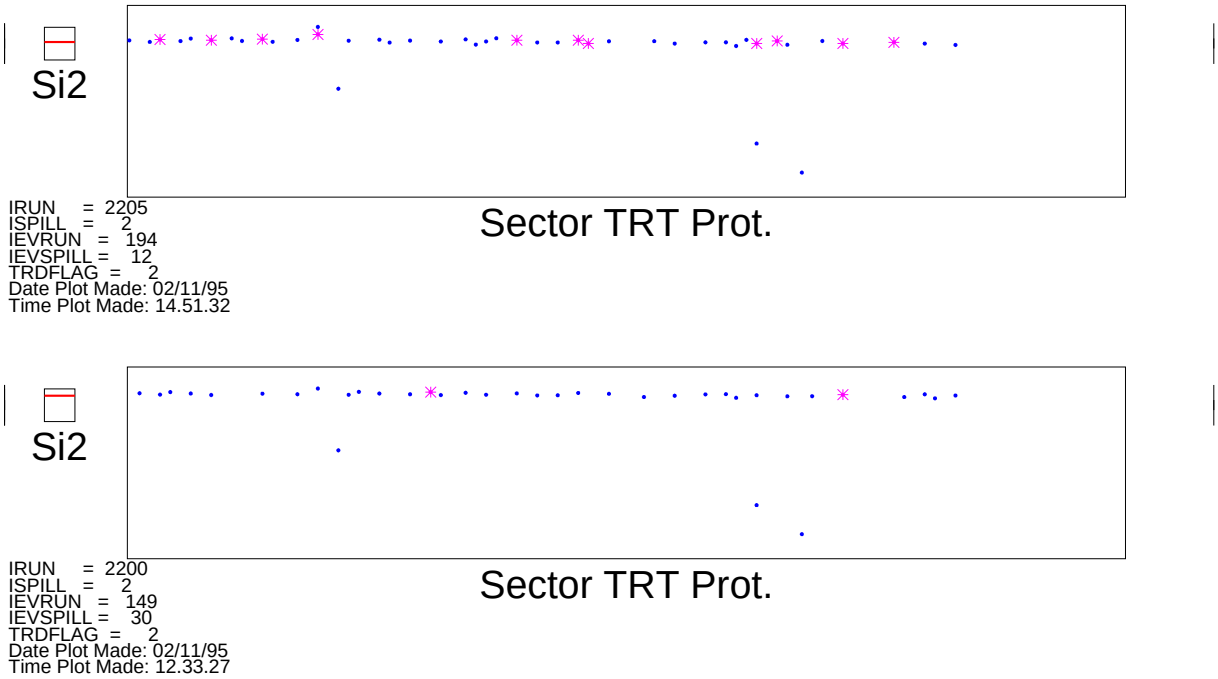

Figure 4.4: An electron(a) and a pion (b) event from the testbeam. Low threshold hits are shown with dots while high threshold hits (TR hits) are shown with stars. Note the large difference in the number of TR hits on the 2 tracks.

rate on the straws .

In the TRDA there are 2 thresholds. The lowest around 300 eV is used to indicate that a charged particle has passed the straw while the second threshold is set in the region of 6 keV and ensures that a transition radiation X-ray has been absorbed in the xenon gas. Both thresholds can be changed using the slow control software in the DAQ system.

Output from the TRDA into the DTMROC provides the time when the anode signal exceeds the first or both thresholds. The TRDS is a service chip which communicates with the slow control to set the thresholds on the TRDA's, mask bad channels and make test pulses.

The DTMROC is the last chip mounted directly on the detector. The chip runs in a loop with a period of 25 ns, equal to the LHC bunch crossing rate. At this level the digital output is formed. If the lower threshold is exceeded at some point during a cycle a bit is set and the time of the rising edge of the signal measured with 3 bit resolution, 0.90 ns. Another bit is set

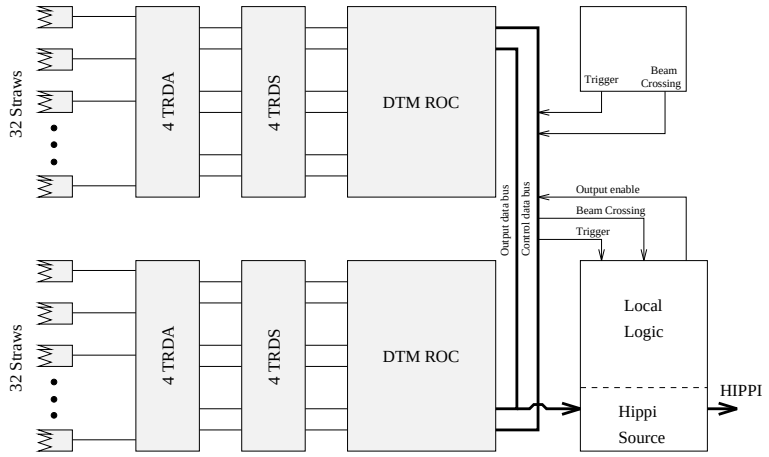

Figure 4.5: The setup of the read out electronics. A signal arrives from an anode wire and runs into the TRDA. Final output is via the HIPPI interface.

if the high threshold is passed. The timing information gives together with the known time of the bunch crossing the drifttime in the straw.

Data is kept in a pipeline structure inside the DTMROC until the trigger system decides if the data should be send to the data acquisition system or discarded.

4.3 Alignment

Alignment of the prototype can be parted into two different problems. Alignment of the straw walls and alignment of the anode wires. The position of the walls determines weather we get a hit or not in the straw from a particle passing the layer. The wire position will determine the relation between drift time and position. A comparison of the two gives a measure on the straightness of the straws. Here will in detail only be described the alignment of the straw walls.

As a first step the external tracking devices are aligned with respect to each other, which makes the path of each particle through the prototype known. As shown in fig. 4.6 the position of the beam along the vertical axis is stored in a histogram for the individual straws each time the given straw has a hit.

Since the straws are not illuminated homogeneously this histogram is normalised to the profile of the beam at the same z position as the straw. This gives a 4 mm wide shadow of the straw which is fitted with a Gaussian

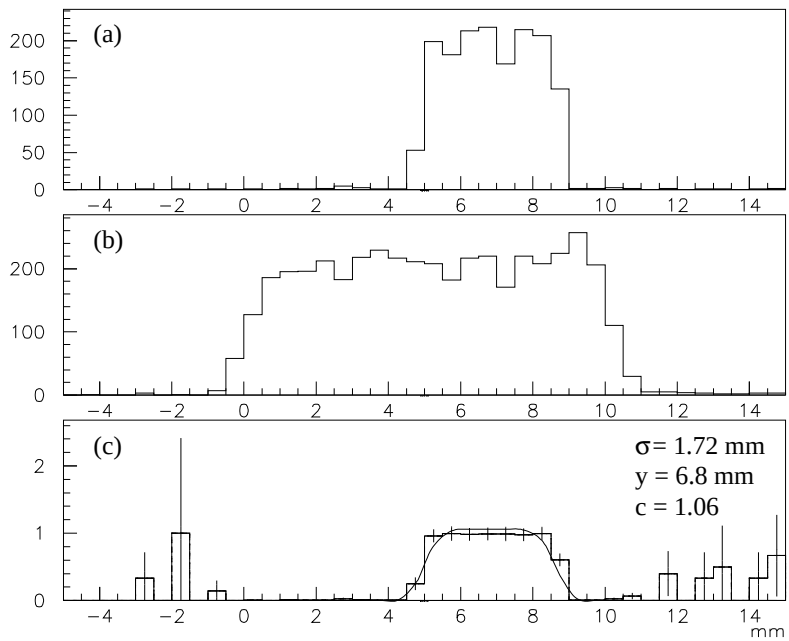

Figure 4.6: The alignment fit of a single straw. (a) shows the profile of the straw along the vertical axis and (b) the beam profile in the same layer as the straw. Finally in (c) the normalised straw profile with errorbars and the fit to the function $ce^{-\frac{1}{2}\left(\frac{y-y_0}{\sigma}\right)^6}$ is shown.

like function

$$f(y) = ce^{-\frac{1}{2}\left(\frac{y-y_0}{\sigma}\right)^6}. \tag{4.1}$$

The process is shown in fig. 4.6.

Now the residual can be defined as the difference between the fitted position and the calculated position from the geometry of the prototype. To avoid wrong results the residue is only calculated for straws with above 100 hits and if c and σ in (4.1) are close to the theoretical values $c = 1.0$ and $\sigma = 2.0$.

The residuals are in fig. 4.7 plotted against the row number of the straw. It is very clear to see that module 4 during the general assembly is placed around 0.5 mm higher than the other modules. Excluding this general misplacement the individual straws have a one standard deviation spread of 250μm. Straws with no calculated residual are assigned an alignment value equal to the mean of the residuals for straws in the same layer.

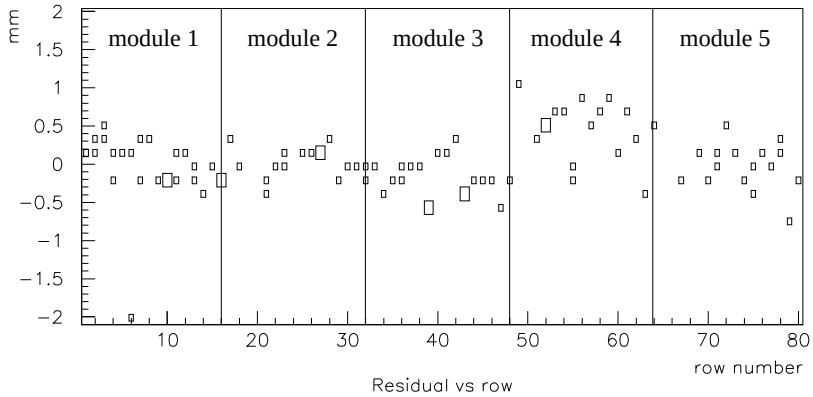

Figure 4.7: The difference between the calculated position of the straws and the position fitted from the external track is plotted along the y axis with the x axis indicating the layer in which the straws are placed. Note that module 4 is placed approximately 0.5 mm higher than the other modules.

The result of the alignment is very clear when looking on the distance of the hits from the reconstructed track in the prototype. With a perfect alignment this will be a plot with a sharp edge at 2 mm and a small tail due to delta rays making hits in a narrow cone around the real track. The same plot before and after the alignment can be seen in fig. 4.8.

All alignment has been done with pions since electrons confuse the procedure by having tracks with kinks because of hard bremsstrahlung. Without the magnetic field the external track was defined by the 2 silicon strip detectors. This was not possible in runs with magnetic field since 1 silicon layer is placed inside the magnet. In this situation the 2 beam chambers and the first silicon layer was used to determine the track in front of the magnetic field.

One may evaluate the precision of the alignment by plotting the evolution in time of the position of individual straws. During a timespan of hours it may be assumed that the detector does not move so the movement in the aligned position is caused only by the precision of the alignment. The best illuminated straws with above 600 hits during a run gives a precision of 40 μm when there was no magnetic field and 70 μm with magnetic field. The alignment is not limited by statistics in the fit but by uncertainties in the external track fit. Since only 1 silicon layer was used for the external track measurement when the magnetic field was on, the resolution is expected to

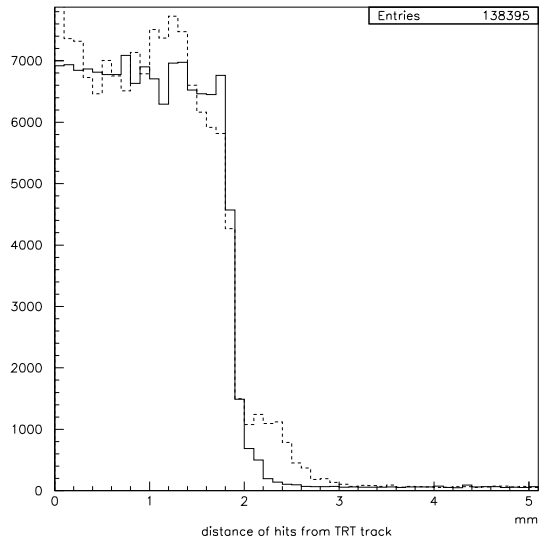

Figure 4.8: The distance from the centre of the straws with hits to the track fitted in the TRT. In dashed line before the alignment and in full line afterwards. Apart from a small tail from delta rays a perfect aligned detector will have a sharp edge at 2 mm. This plot also demonstrates the track fitting capability of the TRT in a stand alone mode.

be worse in the situation with magnetic field.

The evolution in the alignment was monitored during a 42 hour period where the setup was not changed . The main changes in position are common for all straws which indicate a collective movement of the detector or a movement in the devices defining the external track. There are small indications of movement of the individual straws on a scale around 50 μm but the external track measurement is not precise enough to make this observation statistically significant.

4.4 Purity

In the analysis of particle identification it is crucial to have a very good identification of electrons and pions given externally. In the secondary beam a converter of cupper can be inserted which will give a beam mainly of electrons or a large block of plastic which will result in a beam mainly of pions. However especially the electron beam have a very large contamination

of pions and particle identification is needed to exclude pions in the electron beam and visa versa.

The 2 interesting numbers are R_e, the efficiency of finding electrons using the particle identification cuts for pions, and R_π, the efficiency for finding pions using the particle identification cuts for electrons.

R_e is best measured in a beam of dominantly electrons and can be calculated assuming the signals in the multiplicity counter, the Čerenkov counter and the lead glass calorimeter give independent measurements. The efficiency for finding electrons when making cuts for pions is then

$$R_e = \varepsilon_M \varepsilon_{\check{C}} \varepsilon_{LG} \tag{4.2}$$

with ε_M, $\varepsilon_{\check{C}}$ and ε_{LG} indicating the efficiencies of the individual detectors respectively. Measuring the efficiencies would be very easy in a beam containing only electrons but unfortunately the beamline do not provide such a beam. Since the signal in the multiplicity counter cannot be assumed to be fully independent of the signal in the calorimeter it is only used to get a beam with higher concentration of electrons before evaluating $\varepsilon_{\check{C}}$ and ε_{LG}.

A 2-dimensional histogram of the signal from the Čerenkov counter and the calorimeter after an electron cut on the multiplicity counter can be divided into 4 regions as indicated in fig. 4.9. With X_e and X_π defined as the number of electrons and pions in region X

$$X_{total} = X_e + X_\pi = xX_e, \text{ where } x > 1. \tag{4.3}$$

X_{total} is the total number of particles in the region.

Since the cuts on the Čerenkov counter and the calorimeter are assumed independent

$$\varepsilon_{LG} = \frac{D_e}{D_e + C_e} = \frac{1}{1 + \frac{C_e}{D_e}}. \tag{4.4}$$

The fraction of pions in region C will be lower than in region D, so $\frac{d}{c} > 1$ using the notation from (4.3). Inserting this in (4.4) results in an upper limit on the efficiency

$$\varepsilon_{LG} = \frac{1}{1 + \frac{dC}{cD}} < \frac{1}{1 + \frac{C}{D}}. \tag{4.5}$$

However the very large number of particles in region A on fig. 4.9 indicate a very large contamination of pions in the electron beam and (4.5) will be a pessimistic estimate.

The lead glass calorimeter is very well suited for both identifying electrons and pions while the Čerenkov counter do not perform well on electron

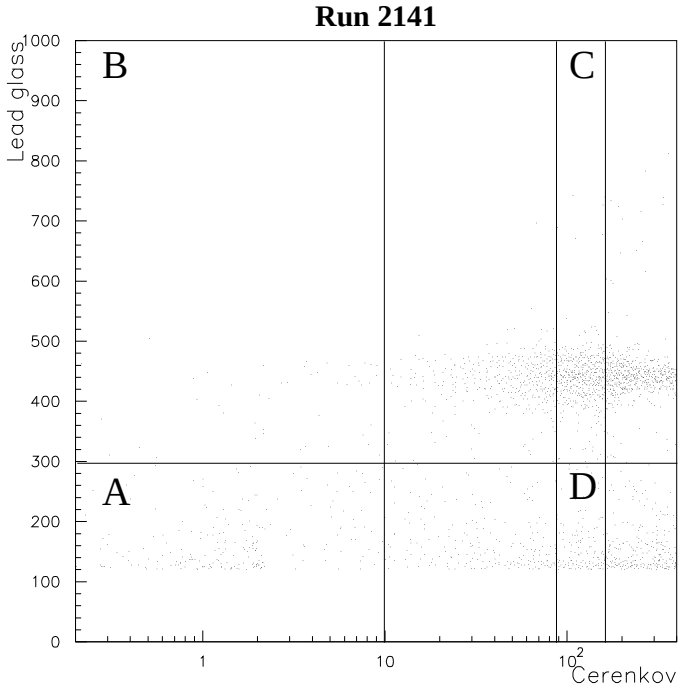

Figure 4.9: Histogram of the signal from a run with predominantly electrons, and where only the particles passing the electron identification cut for the multiplicity counter are filled in. Plotted is the signal in the lead glass calorimeter versus the signal in the Čerenkov counter. The 4 regions indicated are used for estimating the efficiency $\varepsilon_{\mathrm{LG}}$. The many points in region A comes from the very large contamination of pions in the beam.

identification due to a long tail in the distribution from pions as seen in fig. 4.10.

In fig. 4.9 the many particles in the region A indicate a high contamination of pions in the beam. The long tail on the pion distribution results in many pions to the right of region A. To keep d low, region D and C are confined to the interval where most of the electrons give signal from the Čerenkov counter but the ideal situation with $\mathrm{D}_\pi \ll \mathrm{D}_\mathrm{e}$ is far from fulfilled and the estimate (4.5) on $\varepsilon_{\mathrm{LG}}$ will be pessimistic.

The analysis of $\varepsilon_{\check{c}}$ and $\mathrm{R}_\pi < \varepsilon_{\mathrm{LG}}(\pi)\varepsilon_{\check{c}}(\pi)$ are very similar to the calculation of $\varepsilon_{\mathrm{LG}}$ and the results are

$$\mathrm{R}_\mathrm{e} \quad < \quad \varepsilon_{\mathrm{LG}}(\mathrm{e})\varepsilon_{\check{c}}(\mathrm{e}) < 0.014 \cdot 0.032 = 4.4 \cdot 10^{-4} \tag{4.6}$$

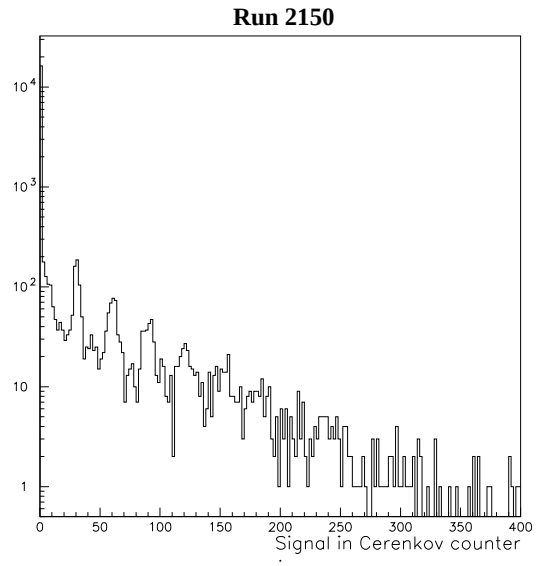

Figure 4.10: The signal from the Čerenkov counter in the case of a beam with almost only pions. It can be seen how noise gives a long tail on the distribution into the area where the signal from electrons lies.

$$\mathrm{R}_\pi \quad < \quad \varepsilon_{\mathrm{LG}}(\pi)\varepsilon_{\check{\mathrm{c}}}(\pi) < 0.0035 \cdot 0.12 = 4.2 \cdot 10^{-4}. \tag{4.7}$$

The conclusion is that the pion beam after external particle identification is pure enough for the electron identification studies where rejections below $5 \cdot 10^{-3}$ are never reached.

4.5 Electron identification

With the alignment of the detector and the purity of the beams under control, the important analysis of electron identification may be done. For data taken with identical setup of field and thresholds, the number of hits above high threshold may be compared for electrons and pions. An example can be seen in fig. 4.11 with a threshold of 7 keV and no magnetic field.

By making a cut on the minimal number of high threshold hits on the track, a curve may be constructed of corresponding efficiencies of pions and electrons including errors as seen in fig. 4.12. The errors are given as statistical errors of one standard deviation. In this plot pion efficiency is a measure of how clean a sample of electrons is obtainable with the TRT prototype

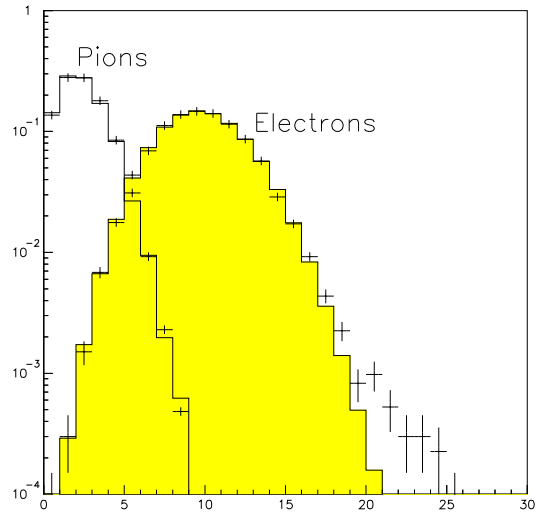

Figure 4.11: The distribution with errorbars of high threshold hits on the tracks for 20 GeV electrons and pions with a threshold at 7 keV, standard gas composition and no magnetic field. A fit is performed with binomial distributions and plotted as histograms. Note the logarithmic scale on the y-axis.

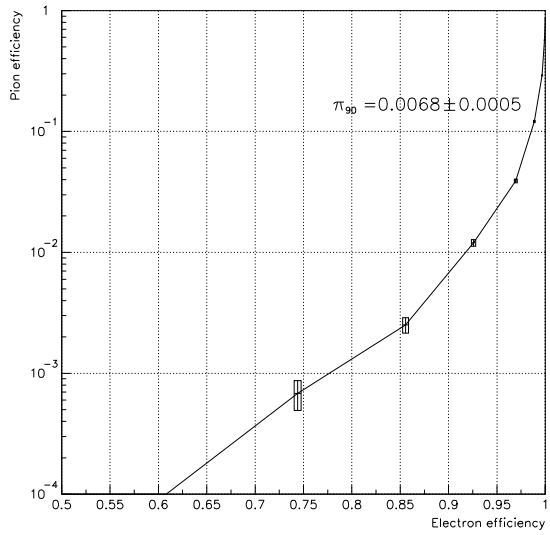

Figure 4.12: A cut on the minimal number of high threshold hits on the track gives corresponding points of electron and pion efficiency. Here they are plotted for 20 GeV pions and electrons with a high threshold at 7 keV, standard gas composition and no magnetic field. π_{90} is the efficiency for finding pions at at electron efficiency of 90%.

alone. Rephrased it measures the fraction of pions identified as electrons by the TRT.

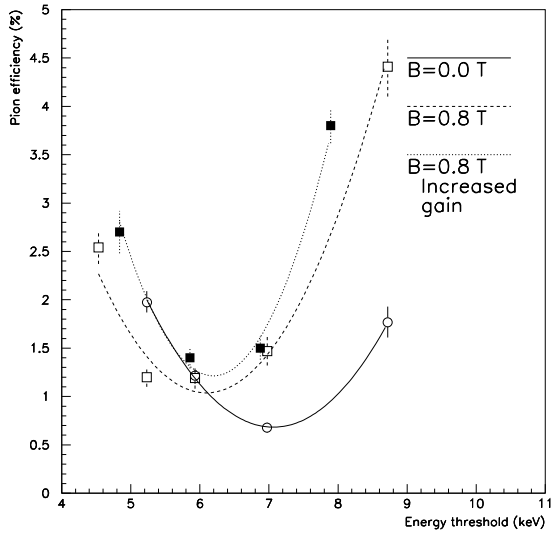

Figure 4.13: The efficiency for pions at different settings of the high threshold. In all measurement points the pion efficiency is plotted at an electron efficiency of 90%. The change in position of the curves with and without magnetic field is commented in detail in the text.

To make comparisons between different settings of high threshold, gas composition and magnetic field the pion efficiency is computed at an electron efficiency of 90%. The curve is constructed as a simple exponential fit between the 2 closest points to 90% including error propagation. The very best rejection power of the prototype is achieved with a high threshold of 7 keV, standard gas composition and no magnetic field and is

$$\varepsilon_\pi = 0.0068 \pm 0.0005 \ @ \ \varepsilon_e = 0.90. \tag{4.8}$$

How different variations of the parameters determine the pion rejection can be see in fig. 4.13. The different curves represent different magnetic fields and different gains in the gas. The curve with a factor 1.37 higher gas gain has been shifted by this factor on the x-axis of the plot.

Comparing the curves with and without magnetic field shows 2 effects, a worse optimal rejection and also a shift in this position from around 7 keV without field to around 6 keV with the 0.8 T field.

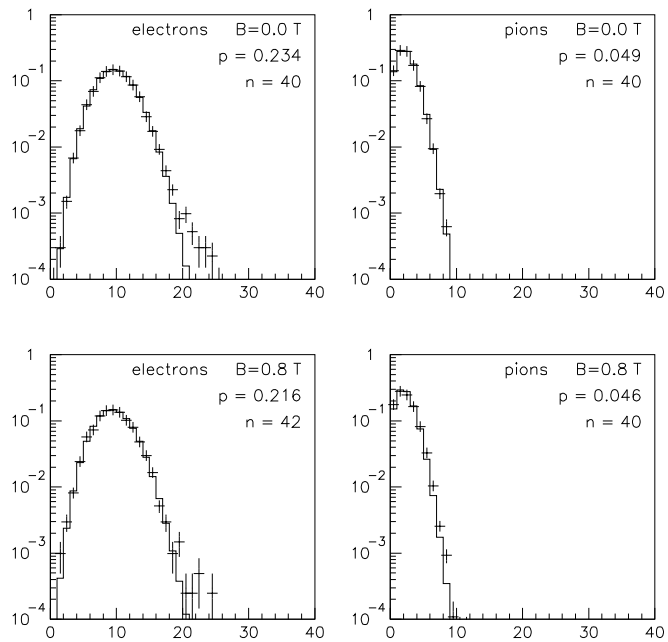

Figure 4.14: Distribution of high threshold hits along pion and electron tracks plotted with a logarithmic y-scale. With error-bars the data and in solid line a binomial fit. The electrons show both with a without field a tail towards more hits coming from bremsstrahlung. For pions a small tail is seen in a magnetic field which is probably due to δ-electrons as explained in the text.

The reason for a worse rejection at optimal threshold in a magnetic field has been the subject of a detailed study. By fitting binomial distributions to the number of high threshold hits as in fig. 4.14 it can be seen that the difference in rejection power comes from a tail in the distribution for pions in magnetic field. With 10% radiation length of material in front of the prototype and only a few percent in the prototype itself pions will only interact by ionisation. A larger number of high threshold hits on the tracks can be explained by δ-electrons curling up around the track with a magnetic field, while they without field can escape from the track.

The spectrum from delta electrons is in [7] given as

$$\frac{\mathrm{d}^2 N}{\mathrm{d}T\mathrm{d}x} = \frac{1}{2} D \frac{Z}{A} \beta^{-2} \rho \frac{F}{T^2}, \tag{4.9}$$

Energy of δ-electron	Average reach (layers)	Radius of curvature (mm)
10 keV	0.10	0.04
100 keV	0.3	0.42
1 MeV	9.4	4.2
10 MeV	280	42

Table 4.1: Properties of δ-electrons created in the endcap prototype.

where $D = 0.307$ MeVcm^{2}g^{-1} is a constant, Z, A, ρ the charge, atomic number and density of the medium, β the velocity of the incoming particle and T the energy of the δ-electron. The factor F is determined by the spin of the incoming particle and given as

$$F = \begin{cases} 1 - \frac{T}{T_{\max}} & \text{spin } 0 \\ 1 - \frac{T}{T_{\max}} + \frac{T}{2E_k^2} & \text{spin } 1/2 \end{cases} \tag{4.10}$$

with $T_{\max}$ the maximum transferable energy in a collision between the incoming particle and an atomic electron. As can be seen in table 4.1 the interesting energy interval is from approximate 10 keV where the δ-electrons created in the foils have a chance to reach the xenon inside the the straws and up to 1 MeV where the electrons escape the prototype. Only above 250 keV will the magnetic field make any difference and for the total prototype (4.9) predicts around 0.8 of those along a pion or electron track. The fraction of those that eventually will dispose enough energy in a single straw to fake a hit from transition radiation can only be predicted by a Monte Carlo simulation of the prototype.

The effect of more δ-electrons staying close to the track in a magnetic field will affect both pions and electrons in exactly the same way since the amount and spectrum of δ-electrons are equal for pions and electrons in the interesting energy interval. However an effect of this size will not show up in the distribution of hits on electron tracks since they already have a tail from bremsstrahlung towards more high threshold hits.

A prediction of the effect of the 2 T field in the ATLAS inner detector can not be predicted from the current data but has to wait for a detailed study with simulations. Two effects come into play. First the effect of δ-electrons as explained above which will worsen the rejection power and second the increase of syncroton radiation from electrons which will improve the rejection power. With the $\frac{1}{E}$ energy spectrum of the δ-electrons there are however very few more electrons to bend in a stronger magnetic field.

The effect of a shifted optimal threshold for pion rejection in a magnetic field compared to no magnetic field do so far not have a satisfactory explanation. Since the magnet is not superconducting the temperature in the prototype was around 8K higher with the field on and maybe large temperature gradients play a role. The gain was monitored on straws at a different position to the ones where the particles passed through, maybe resulting in a wrong calibration of the gain. This would give a wrong translation to the keV scale on the x-axis of fig. 4.13. Results from the 1996 run in a 2 T superconducting magnet will not be affected by such problems and can also be used to further study the relationship between rejection of pions and magnetic field.

4.5.1 Dependence on detector length

The pion efficiency is affected strongly by the length of the detector. To have a shorter detector or simply just ignore the data in the last layers of the prototype give the same effect. In fig. 4.15 is shown the connection between detector length and pion efficiency for particles without a magnetic field and at the optimal threshold of 7 keV. The deviations of the curve from a pure exponential connection between pion efficiency and detector length are not connected to the physical parting of the prototype in 5 independent sections and are the same both with and without magnetic field.

A close look on the first part of the curve in fig. 4.15 shows very clearly that it takes around 100 mm of the detector to build up the full rejection power. This is mainly caused by X-rays passing through several layers before they are absorbed in a straw. From fig. 3.7 it is clear that only the X-rays with the highest energies can travel this far in the detector before absorption.

A plot of the hit frequency in each plane of straws as in fig. 4.15 show certain planes where the readout electronics has a lower performance. The general slope comes from the 19.2° rotation of the prototype (see fig. 4.1). The sharp drops in the frequency are caused by problems with the readout electronics. It is an electronics problem and is a common problem for a plane and not connected to just single straws. Comparing the two plots in fig. 4.15 shows that the deviations from an exponential behaviour of pion efficiency with detector length is entirely caused by electronics with low efficiency.

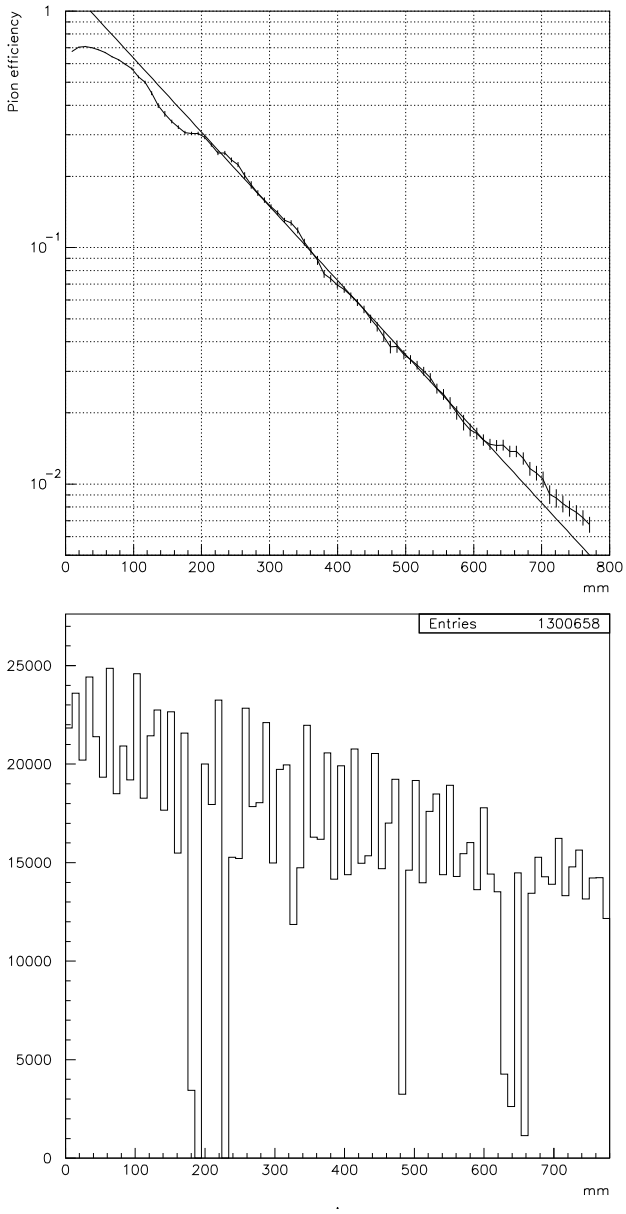

Figure 4.15: In the first plot the pion efficiency for different lengths of the prototype. The exponential fit is performed for the points between 200 and 600mm. In the second plot the frequency of hits in the individual straw planes. The general slope comes from the beam going through the detector such that the seen distance of the straws increases through the detector. Note how the imperfect electronics coincide exactly with the positions where no additional rejection is obtained.

Chapter 5

Simulation and reconstruction

5.1 Physics simulation

The physics event is for all physics here simulated with the PYTHIA [8, 9] program package. From an input of two 7 TeV protons colliding with proper structure functions it simulates the creation of particles in the scattering process. Normally this is divided into 2 parts.

- **The hard scattering**. With specific datacards PYTHIA can be forced to create specific hard scattering events like Higgs production or $t\bar{t}$ pairs.
- **Minimum bias**. Here all kind of events are created with the proper cross section, which means the simulated events are entirely dominated by QCD scattering. Hence mainly bunches of hadrons are created, usually with no high p_{T} jets.

5.2 Detector simulation

In the GEANT volume structure the complete design of the detector is described with the highest degree of precision. The GEANT [10] package can then simulate the movement of the particles through the different sub detectors. Effects like conversion, multiple scattering, decay of long lived particles, bremsstrahlung and transition radiation are simulated, and the energies stored in all materials are calculated. A detector simulation can either be performed on physics events as described in the previous section or on single particles.

5.3 Detector response

The next step in the long simulation chain is to compute the response to the deposited energy of the individual detection element (a straw in the TRT or a calorimeter cell). At this level several events in the same bunch crossing can no longer be treated individually so one has to take the luminosity into account. This is done by adding minimum bias events on top of the main event. Those are GEANT simulated individually but are now joined together. The number of events put on top of the main event are Poisson distributed with a mean given by the luminosity.

At the end of this step the data from the simulation and real data from the experiment have the same digital format.

5.4 Triggering

It can at this step be determined if the simulated event will pass all the trigger levels and continue to reconstruction. While the trigger algorithms for simulated and real data of course are supposed to be the same the data management is very different since the data in the simulation are not distributed physically over the detector as will be the case for ATLAS.

5.5 Reconstruction

With events passing the trigger one tries to reconstruct the physics event we started with but only using the simulated detector response.

The 3 main parts are track finding in the muon system, cluster finding in the calorimeters and track finding in the inner detector. The process of finding the tracks or clusters is often called pattern recognition. At the present stage of the ATLAS reconstruction code many parts are not fully developed and other parts like track finding exist in several parallel forms with individual advantages.

The main part of the work described in chapter 6 have used a package for pattern recognition and track fitting in the inner detector combining a Hough transform and the Kalman filter method. Only this package and the software developed for conversion identification will be described in more detail.

5.6 Pattern recognition and track fitting

The program for pattern recognition and track fitting in the Inner detector is partly described in the note [11] by Igor Gavrilenko who has also developed the code. The strategy is to perform the initial pattern recognition in the TRT and then afterwards use the information from the precision detectors. This may seem strange with the high occupancy in the TRT but the large number of hits on each track, above 28 except for tracks in the crack between barrel and endcap TRT, makes a method using histograms very efficient for pattern recognition.

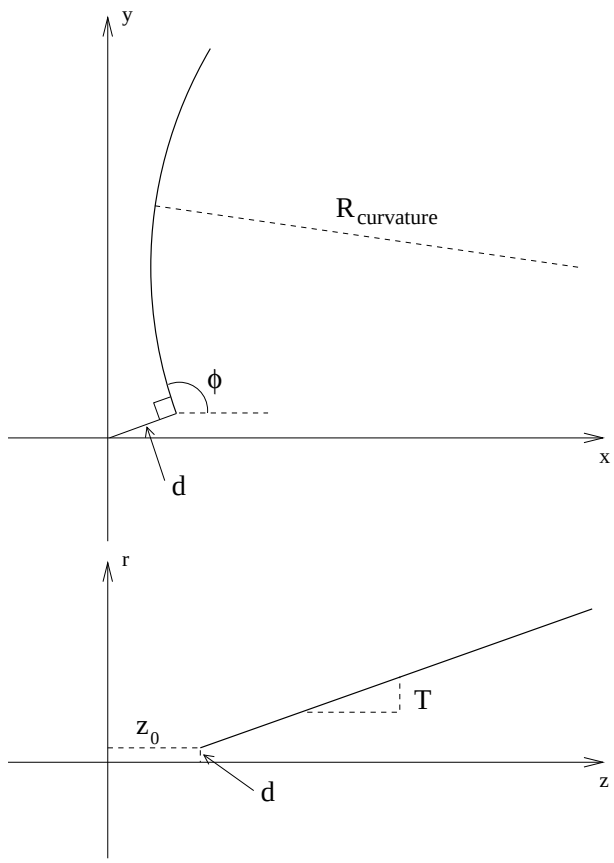

Figure 5.1: The parameters describing a helix in a solenoidal field. Often is used the curvature $C = 1/\mathrm{R}_{\mathrm{curvature}}$ instead of the radius of curvature directly.

The special method called a Hough transform uses a table of coordinates

$\varphi(r, C)$ for tracks having parameters

$$(d, z_0, \varphi_0, C) = (0, 0, 0, C) \tag{5.1}$$

with the parameters defined as seen in fig. 5.1. The curvature is given in equal steps in the interval $[-C_{max}, C_{max}]$ and

$$C_{max} = \frac{B}{333\, p_{\mathrm{T}_{min}}}, p_{\mathrm{T}_{min}} = 0.5 \text{ GeV} \tag{5.2}$$

with B the magnetic field measured in Tesla.

For each curvature all the hits in the TRT are now shifted in the φ coordinate with the value $\varphi(r, C)$. This makes track finding a matter of finding lines with many hits on at constant φ. All hits are sorted in the new φ coordinate and a simple counting algorithm can make a continuous scan in φ. This method bins the hits in the searched curvatures but not in φ_0 and gives the Hough transform an advantage to a straightforward approach, where all hits are filled into a 2-dimensional histogram with bins in (R, φ), and straight lines are searched.

The shifting in φ is now repeated for the next curvature and since the shift in φ from one curvature to the next is very small the φ coordinates will to a large extend still be in order making sorting in the new φ fast.

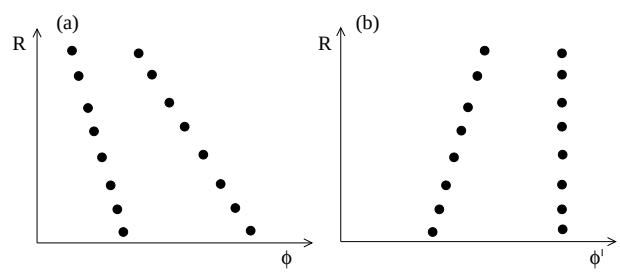

Figure 5.2: In (a) are seen hits in the TRT from tracks with 2 different curvatures. In (b) the same hits after the Hough transform with the correct curvature for one of the tracks. Note how hits line up at the same φ'.

The method given here works in the barrel TRT while for the endcap TRT all R coordinates needs to be replaced by the z coordinate of the straws and the scanning will be in C/T and not C. It simply reflects the 2 different projections the hits are measured in for the barrel and the endcap TRT. An illustration of the Hough transform is given in fig. 5.2 and the result of a single scan in φ can be seen in fig. 5.3. The stability of the Hough transform at high luminosities has been proven in [12] where it is shown that

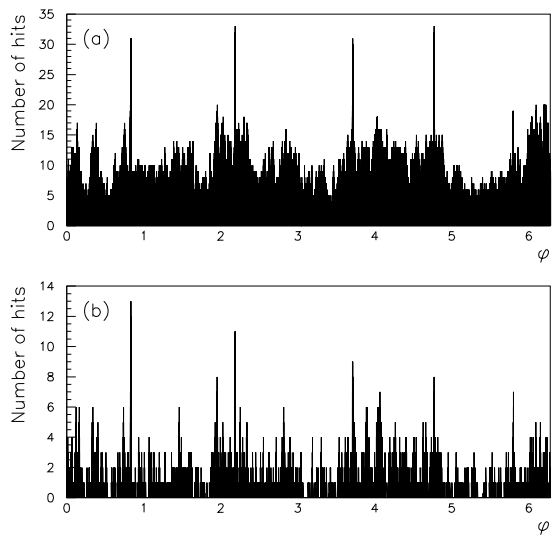

Figure 5.3: A scan for a single curvature of tracks in a simulation with 20 GeV electrons. The high p_{T} tracks are clearly seen above the background from low p_{T} tracks. All hits in the TRT are plotted in (a) while only hits above the high threshold are plotted in (b).

the rate of fake tracks is well below the rate of real tracks in the pile-up at all luminosities. With fake tracks is meant tracks identified by the Hough transform with no counterpart in the simulated tracks.

The track candidates from the Hough transform can now be used as seeds for continued pattern recognition and precision fitting in the Silicon detectors. A Kalman filter approach is used but the special algorithm is so far undocumented. The basic principles of Kalman filtering for track fitting can be found in [13].

After the final Kalman filter the track is in the August 1995 version of the program parametrised as

$$\bar{p} = \begin{pmatrix} x \\ y \\ z \\ \varphi \\ \cot T \\ C \end{pmatrix} \tag{5.3}$$

where T and C are shown in fig. 5.1. φ is here the direction of the track

in the point (x, y, z). The error matrix V is described at the point (x, y, z) where either x or z is regarded as a fixed coordinate given a reference surface. The reference surface will always coincide with a detector surface. A global rotation of the system with the angle φ_0 around the z axis is also allowed such that all detecting elements can be described as either a fixed x or a fixed z surface.

5.7 Reconstruction of conversions

A new package of software has been written with the special purpose to reconstruct conversions. It uses many of the ideas developed for vertex fitting in B-physics and is a variant of the Kalman filtering method. It can be divided into three steps. First a vertex fit where a common vertex between two tracks, the conversion point, is found. Then second, a kinematical fit for the two electrons to come from a converted photon, and third a fit for the reconstructed photon to point back towards the primary vertex. All steps are important both to improve the momentum resolution of the converted photon and to reject fake conversions.

5.7.1 The vertex fit

From the track reconstruction the parameters $\vec{p_i}$ of the tracks including error matrices G_i are known at some reference surfaces. The idea of a vertex fit is to find a common point $\vec{x}$ in space where tracks with parameters $\vec{q_i}$ propagate to the known parameters on the reference surface as illustrated in fig. 5.4. The step from fit parameters $(\vec{x}, \vec{q_i})$ to parameters on the reference surface can be described by the known mapping $\vec{h_i}$. In this formulation the purpose of a vertex fit is to find $(\vec{x}, \vec{q_i})$ such that

$$\vec{p_i} = \vec{h_i}(\vec{x}, \vec{q_i}) + \vec{\varepsilon_i} \tag{5.4}$$

and $\vec{\varepsilon_i}$ is minimised for all tracks from a common vertex simultaneously.

The maps $\vec{h_i}$ are not invertible and also the error matrices on each track and independent information on the vertex needs to be taken into account. Hence the problem is quite complicated. In the Kalman filter method (5.4) is regarded as a measurement equation where $\vec{\varepsilon_i}$ is a noise term. The problem is solved by making a linear approximation to $\vec{h_i}$,

$$\vec{h_i}(\vec{x}, \vec{q_i}) = A_i \cdot \vec{x} + B_i \cdot \vec{q_i} + \vec{c_i}^{(0)} \tag{5.5}$$

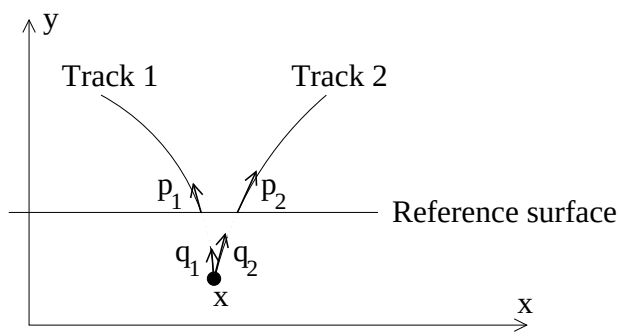

Figure 5.4: Before the vertex fit the track parameters $\vec{p_i}$ are known at some fixed reference surface. The vertex fit determines the vertex position x and the track parameters $\vec{q_i}$ at the vertex, closest matching the parameters $\vec{p_i}$ at the reference surface.

where

$$A_i = \left.\frac{\partial \vec{h_i}}{\partial \vec{x}}\right|_{\vec{x}^{(0)},\vec{q_i}^{(0)}} \tag{5.6}$$

$$B_i = \left.\frac{\partial \vec{h_i}}{\partial \vec{q_i}}\right|_{\vec{x}^{(0)},\vec{q_i}^{(0)}} \tag{5.7}$$

$$\vec{c_i}^{(0)} = \vec{h_i}(\vec{x}^{(0)}, \vec{q_i}^{(0)}) - A_i \cdot \vec{x}^{(0)} - B_i \cdot \vec{q_i}^{(0)}. \tag{5.8}$$

$\vec{x}^{(0)}$ is the initial best guess on the vertex position and the kinematical part of $\vec{p_i}$, $(\varphi, \cot T, C)^\top$ from (5.3), used as $\vec{q_i}^{(0)}$.

For a vertex fit to a conversion, $\vec{x}^{(0)}$ is the position of the hit closest to the primary vertex of all the hits on the two tracks. The covariance matrix $C_0 = \mathrm{Cov}(\vec{x}^{(0)})$ describes the precision of the initial guess independent of the track parameters.

$$C_0 = \begin{pmatrix} d_{\mathrm{det}}^2 & 0 & 0 \\ 0 & \infty & 0 \\ 0 & 0 & \infty \end{pmatrix} \tag{5.9}$$

with d_{det} the thickness of the layer at $\vec{x}^{(0)}$. The C_0 in (5.9) describes the situation with a fixed x coordinate of the track parameters (5.3).

In the filtering step of the Kalman filter the tracks are added one at a time to the initial vertex and an update on both vertex position and kinematic parameters can be calculated using the following expression

$$W_i = \left(B_i^\top G_i B_i\right)^{-1} \tag{5.10}$$

$$
\begin{aligned}
G_i^B &= G_i - G_i B_i W_i B_i^\top G_i && (5.11)\\
C_i &= \left(C_{i-1}^{-1} + A_i^\top G_i^B A_i\right)^{-1} && (5.12)\\
\vec{x_i} &= C_i \left(C_{i-1}^{-1} \vec{x_{i-1}} + A_i^\top G_i^B \left(\vec{p_i} - \vec{c_i}^{(0)}\right)\right) && (5.13)\\
\vec{q_i} &= W_i B_i^\top G_i \left(\vec{p_i} - \vec{c_i}^{(0)} - A_i \vec{x_i}\right). && (5.14)
\end{aligned}
$$

C_i is the covariance matrix on the vertex position $\vec{x_i}$ after track i has been added. $\vec{q_i}$ is the updated kinematic parameters of track i restricted to the best vertex of the first $i-1$ tracks and $\vec{x_i}$ the new vertex position. The updated track parameters (5.10) are derived from the requirement to minimise the χ^2 from adding the track i.

$$
\begin{aligned}
\chi_i^2 = &\left(\vec{p_i} - \vec{c_i}^{(0)} - A_i \vec{x_i} - B_i \vec{q_i}\right)^\top G_i \left(\vec{p_i} - \vec{c_i}^{(0)} - A_i \vec{x_i} - B_i \vec{q_i}\right) + \\
&\left(\vec{x_i} - \vec{x_{i-1}}\right)^\top C_{i-1}^{-1} \left(\vec{x_i} - \vec{x_{i-1}}\right). && (5.15)
\end{aligned}
$$

The first part of the expression for the χ^2 determines how well the new helix fit with the original from $\vec{p_i}$ and the second part how well the new vertex position fits with the vertex position from last iteration. A strict derivation of the vertex fit can be found in [14].

For the second track in the conversion all kinematic parameters are fully updated with information on the vertex position from $\vec{x}^{(0)}$ and $\vec{p_1}$ while the first track never uses the information from $\vec{p_2}$. The smoother part of the Kalman filter takes care of this by updating the $n-1$ first tracks in a vertex fit to use the best vertex position x_n. For a conversion it is only the first track that need to be smoothed and

$$
\vec{q_1} = W_1 B_1^\top G_1 \left(\vec{p_1} - \vec{c_1}^{(0)} - A_1 \vec{x_2}\right). \qquad (5.16)
$$

Finally the covariance and correlation matrices are

$$
\begin{aligned}
F_i &= W_i B_i^\top G_i A_i \\
E_i &= -F_k C_2 \\
\mathrm{Cov}(\vec{q_i}) &= W_i - E_i F_i^\top && (5.17)\\
\mathrm{Cor}(\vec{x}, \vec{q_i}) &= E_i && (5.18)\\
\mathrm{Cor}(\vec{q_i}, \vec{q_j}) &= F_i C_2 F_j^\top && (5.19)
\end{aligned}
$$

The linear approximation of (5.4) in (5.5) makes it necessary to iterate the vertex fit. In the k'th iteration the position and correlation matrix of the $(k-1)$'th iteration are used as $\vec{x}^{(0)}$ and C_0. The iteration is continued until either the total $\chi^2 = \chi_1^2 + \chi_2^2$ stabilises or a maximum iteration number is reached.

If the final χ^2 is large it can be caused by a wrong assumption in the initial guess on the correlation matrix C_0 for the vertex position. Hence for large χ^2 values the complete vertex fit is repeated with C_0 infinite in all diagonal elements corresponding to no a priori information on the vertex position.

5.7.2 The mass constraint fit

A conversion is not only identified by a common vertex between an electron and a positron but also by the two particles 4-momenta adding up to the 4-momenta of a zero mass photon. An equation g in the parameter $\vec{\alpha} = (\vec{x}, \vec{p_1}, \vec{p_2})^\top$,

$$g(\alpha) = E_1 E_2 - \vec{p_1} \cdot \vec{p_2}, \tag{5.20}$$

which is zero for a conversion, can be used to make a constraint fit on the electron positron pair. The fit is however more stable if the kinematical constraint (5.20) is divided into two geometrical constraints

$$\vec{g}(\vec{\alpha}) = \begin{pmatrix} p_{x_1} p_{y_2} - p_{x_2} p_{y_1} \\ \frac{p_{\mathrm{T}_1}}{p_{z_1}} - \frac{p_{\mathrm{T}_2}}{p_{z_2}} \end{pmatrix} \tag{5.21}$$

requiring the outgoing electron and positron to be parallel both in the transverse and longitudinal projection. Again by making a linear approximation an improved value of the parameters, $\vec{\alpha}_m$, can be obtained by minimising

$$\chi^2 = (\vec{\alpha}_m - \vec{\alpha})^\top V_\alpha^{-1} (\vec{\alpha}_m - \vec{\alpha}) + 2\vec{\mu}^\top \vec{g}(\vec{\alpha}_m) \tag{5.22}$$

where $\vec{\alpha}$ are the parameters from the vertex fit with covariance matrix V_α and $\vec{\mu}$ is a vector of Lagrange multipliers introduced to make a minimisation including the constraint from (5.21).

A linear approximation is obtained by expanding $\vec{g}$ around a best estimate $\vec{\alpha}^{(0)}$ of $\vec{\alpha}$,

$$\vec{g}(\vec{\alpha}) = \vec{g}(\vec{\alpha}^{(0)}) + \Gamma \cdot (\vec{\alpha} - \vec{\alpha}^{(0)}) \tag{5.23}$$

with Γ defined as

$$\Gamma = \left. \frac{\partial \vec{g}}{\partial \vec{\alpha}} \right|_{\vec{\alpha}^{(0)}}. \tag{5.24}$$

Now the minimum of (5.22) can be found from the derivates

$$\frac{\partial \chi^2}{\partial \vec{\alpha}_m} = \Gamma(\vec{\alpha}_m - \vec{\alpha}) + \Gamma V_\alpha \Gamma^\top \vec{\mu} = 0 \tag{5.25}$$

$$\frac{\partial \chi^2}{\partial \vec{\mu}} = \Gamma(\vec{\alpha}_m - \vec{\alpha}^{(0)}) + \vec{g}(\vec{\alpha}^{(0)}) = 0. \tag{5.26}$$

where $\vec{\mu}$ can be extracted

$$\vec{\mu} = \left(\Gamma V_\alpha \Gamma^\top\right)^{-1} \left(\vec{g}(\vec{\alpha}^{(0)}) + \Gamma(\vec{\alpha} - \vec{\alpha}^{(0)})\right) \tag{5.27}$$

and inserted into (5.25) yielding

$$\vec{\alpha}_m = \vec{\alpha} - V_\alpha \Gamma^\top \left(\Gamma V_\alpha \Gamma^\top\right)^{-1} \left(\vec{g}(\vec{\alpha}^{(0)}) + \Gamma(\vec{\alpha} - \vec{\alpha}^{(0)})\right) \tag{5.28}$$

Due to the linear approximation of $g(\vec{\alpha})$ in (5.23) the result obtained for $\vec{\alpha}_m$ need to be iterated with the expansion point $\vec{\alpha}^{(0)}$ set to $\vec{\alpha}_m$ from the previous iteration but α should still be the parameters obtained from the vertex fit. As in the case of the vertex fit the iteration continuous until the χ^2 given as

$$\chi^2 = \left(\vec{g}(\vec{\alpha}^{(0)}) + \Gamma(\vec{\alpha} - \vec{\alpha}^{(0)})\right)^\top \left(\Gamma V_\alpha \Gamma^\top\right)^{-1} \left(\vec{g}(\vec{\alpha}^{(0)}) + \Gamma(\vec{\alpha} - \vec{\alpha}^{(0)})\right) \tag{5.29}$$

stabilises or a maximum number of iterations are reached. Finally the covariance matrix for the mass constrained vertex is given as

$$V_{\alpha_m} = V_\alpha \Gamma^\top \left(\Gamma V_\alpha \Gamma^\top\right)^{-1} \Gamma V_\alpha. \tag{5.30}$$

5.7.3 Photon from primary vertex

For LHC the spread in the position of the primary vertex, where the hard scattering of gluon or quarks from the colliding protons happen, is planned to be very small in the transverse plane but with a larger spread along the beams. The currently believed parameters are

$$\sigma_{\mathrm{T}} = 15\mu\mathrm{m} \tag{5.31}$$

$$\sigma_z = 6.5\mathrm{cm} \tag{5.32}$$

Since the interesting photons, which later can convert, all come from the primary vertex, the small spread on this give another handle on the identification and reconstruction of converted photons.

As for the other fits used the Kalman filter approach the idea is to construct a χ^2 function and then minimise a linear approximation to this. The method is not fully developed for ATLAS yet and results are not conclusive. The work has so far been done using the ideas described in the note [15].

Chapter 6

Physics potential of electron identification

6.1 B-physics

At low luminosity the B-physics will be one of the dominant subjects for the ATLAS detector. B-physics span a wide range of processes where the main part will be

- CP-violation in the B-system mainly through the processes $B_d^0 \rightarrow J/\Psi\, K_s^0$ and $B_d^0 \rightarrow \pi^+\, \pi^-$.
- Rare decays like $B_d^0 \rightarrow \mu^+\, \mu^-$. This clean signal is predicted with a very low branching ratio in the standard model and a larger branching ratio will be an indication of some new physics.
- Mixing in the $B_s^0\, \bar{B}_s^0$ system.

Common for all those channels are the low energies involved. The general level 1 trigger for B-physics will be an isolated muon above 6 GeV p_T. This level 1 trigger is chosen since it to a very large extend suppress the background from lighter quark events and gluon fusion processes. Since the jet structure is very spread out in low energy events, there will be no RoI's defined for the level 2 trigger. The p_T limit is pressed as low as the rate of events will allow. A direct J/Ψ trigger is not possible at level 1 since the read out from the TRT will arrive too late. For the CP-violation studies in the $B_d^0 \rightarrow J/\Psi\, K_s^0$ system, the TRT will play a vital role in the Level 2 trigger since the Hough transform can be performed at this level to identify pairs of electrons from J/Ψ decay.

After the 6 GeV p_T muon trigger the background consist almost entirely of events containing at least 2 b-quarks. The electron pairs passing the trigger in the TRT can be divided into 3 groups

h^+h^- Two hadrons from the underlying event or the pile-up are reconstructed as electrons.

$e^\pm h^\mp$ A real electron and a hadron faking an electron of opposite sign make a pair.

e^+e^- A real electron pair. In this group there will still be a large background from photon conversions.

The first two backgrounds can be reduced by a cut on the fraction of transition radiation hits in the TRT.

$$\begin{aligned} r_i &= \frac{\#\text{ TR hits on track i}}{\#\text{ hits on track i}} \\ R &= \frac{\#\text{ TR hits on both tracks}}{\#\text{ hits on both tracks}}, \end{aligned} \tag{6.1}$$

while the background from conversions require a more sophisticated job. If photons convert inside the barrel TRT they can easily be identified by the lack of hits in the innermost layers. This is not possible in the endcap TRT, where the radial coordinate is not reconstructed.

The real electron pairs selected by the J/Ψ trigger will have a large background from photon conversions. With the relatively poor momentum reconstruction at the trigger level it is not possible to make a cut on $m_{e^+e^-}$. Also rare decays like $B^0_{d,s} \to e^+e^-$ and $b \to se^+e^-$ where the electron pair is non-resonant are open for the trigger when no cut is made on the invariant mass of the J/Ψ candidate. Many conversions happen outside the 2 innermost pixel layers and hence a requirement on hits in a pixel layer from the electron tracks will reduce the conversion background strongly but have a rather small effect on the J/Ψ signal. However it is not likely that combined tracking in the silicon layers and the TRT can be done in the short CPU time available at the level 2 trigger.

After the level 1 trigger there will be an approximate rate of 4 kHz. From a study [16] in the pseudorapidity region below 0.8 it has been shown that in each event passing the level 1 trigger 0.15 e^+e^- pairs are reconstructed mainly originating from conversions and semileptonic decays. No vertexing is done at this level of reconstruction and hence a pair is defined just as two reconstructed particles of opposite charge. The background after the level 1 trigger is in mean 33 pairs with either one or two hadrons in each event.

From this it can be seen that it for a level 2 trigger is absolutely essential to have particle identification. The energies are in general low leading to a limited use of the calorimeter to identify electrons and the TRT will be the only device to reduce background from hadrons.

The full simulation study [16] in the central rapidity region with the barrel TRT shows a background rate of 470 ± 40 Hz with an efficiency for J/Ψ from B_d^0 decays of $90 \pm 3\%$ using the cuts

$$\begin{aligned} r_i &\geq 0.10 \\ R &\geq 0.18 \\ p_T &\geq 0.5 \text{ GeV}/c \end{aligned}$$

together with removal of conversions starting inside the TRT. Changing the lower limit on reconstructed transverse momenta to 1 GeV/c reduces the background rate to 270 ± 30 Hz with an efficiency of $86 \pm 3\%$.

Extrapolation to the full range of pseudorapidity below 2.5 using simulations at particle level results in a rate after the level 2 J/Ψ trigger of 550 ± 40 Hz using all tracks above 1 GeV/c. This rate is only slightly above the rate of 400 Hz reserved for the J/Ψ channel in the ATLAS technical proposal [1] after level 2 and shows that a trigger for electron pairs in ATLAS is possible.

It is clear that the TRT is absolutely essential for the decay channel $B_d^0 \to J/\Psi K_s^0$ with $J/\Psi \to e^+e^-$ and thereby doubling the statistics compared to only using the decay $J/\Psi \to \mu^+\mu^-$.

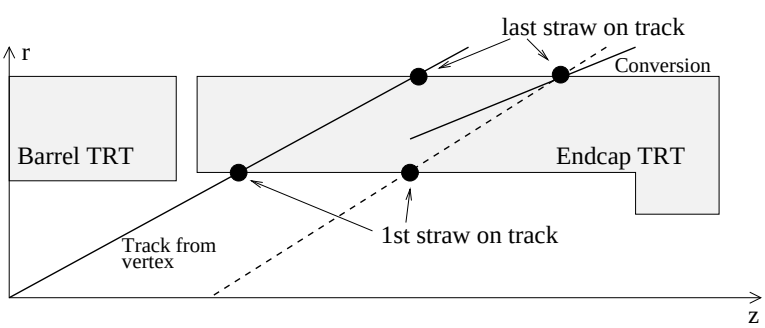

Figure 6.1: A quarter view of the TRT. In the endcap a tracks slope and crossing with the z-axis is inferred from the entry and exit point of the TRT. A conversion will as shown with a dashed line fake a track with a displaced vertex.

Several uncertainties are connected to the extrapolation for the full detector from results in the barrel TRT as done in [16]. Rejection of conversions

will be more difficult due to the geometry. In the barrel TRT all tracks from the primary vertex pass through all layers of straws and the conversions inside the TRT can be identified by not having hits in the innermost layers. In the endcap where tracks are found in a $\phi - z$ projection and tracks do not pass through all layers conversions need a good identification of both entry and exit point of the detector as shown in fig. 6.1 and hence the rejection of conversions will not be as powerful as in the barrel TRT.

Also tracking in the region where tracks are partly in the endcap and partly in the barrel will give special problems for the pattern recognition when the silicon tracker is not included. The number of hits on the tracks are low and are shared on two track segments in different projections.

6.2 Conversions in the $\mathrm{H} \rightarrow \gamma\gamma$ channel

To find a Higgs particle with a mass below 130 GeV will be very difficult at LHC. The Higgs particle will as the mass creating particle couple to other particles proportional to their mass. The effect of this is that a standard model Higgs always will decay dominantly to the heaviest possible particles. For $m_{\mathrm{H}} < 2m_{\mathrm{W}}$ the dominant decay will be $\mathrm{H} \rightarrow \mathrm{b}\bar{\mathrm{b}}$ but as discussed in section 6.5 this is a very difficult decay to detect because of the huge background from QCD jets. Another slightly more favourable decay is the decay through two virtual top quarks to two photons as shown in fig. 6.2 or in a similar process through a virtual W pair. The main production of Higgs happens in a process called gluon fusion as shown in the same figure.

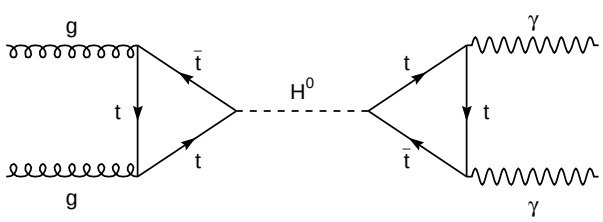

Figure 6.2: The dominant Higgs production through gluon fusion and the decay to 2 photons.

The calculated branching ratios for decay of a standard model Higgs can be seen in fig. 6.3. The branching ratio to two photons fall out the bottom of the figure but is estimated to 0.0012 for a Higgs mass of 90 GeV and follows in shape the branching ratio to two gluons.

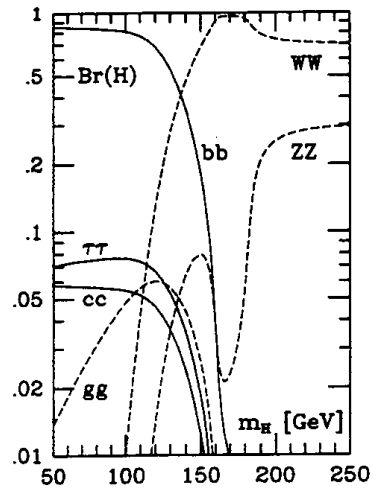

Figure 6.3: Branching ratio for standard model Higgs decay. The decay to two photons falls below the bottom of the figure. From [2].

To detect final states with two photons at LHC conditions sets very high requirements on the detector. Reducible background comes from both QCD jets and isolated electrons faking photons. Electrons will especially be a problem for a Higgs mass close to the mass of the Z^0 where the background from $Z^0 \rightarrow e^+e^-$ is resonant. The background has a rate around 25.000 times higher than the $H \rightarrow \gamma\gamma$ signal. The background from misidentified jets will be considerable larger but will not be resonant at any specific invariant mass and is thus less dangerous.

QCD jets are rejected by using the calorimeters in almost the same way as for the electron identification described in section 6.3. The remaining jet background faking photons consist almost entirely of a π^0 carrying the major part of the energy. Since the π^0 decay immediately to two photons the background is difficult to reduce. Within the calorimeter the fine grained preshower is able to provide between a factor two and three of rejection by discriminating on the width of the energy deposition in the η direction. Details on the method used can be found in [17]. However for identified conversions this can be done better by reconstructing the tracks and constructing the ratio

$$R = \frac{\sum_{i=1}^{2} p_{\mathrm{T}_i}}{E_{\mathrm{T}}} \tag{6.2}$$

with the sum over the two tracks in a conversion. For single photons R will be close to unity while for pions the sum of transverse momenta only adds up for one of the pions giving R below 1. No full simulations has been done

on the use of R for γ/π^0 separation, but this will be the next area to look at with the conversion algorithm.

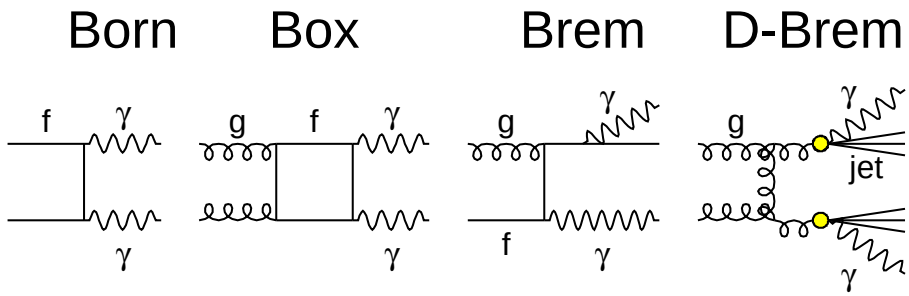

Figure 6.4: Irreducible background to the two photon decay of a Higgs boson from the Born process, box diagrams, single bremsstrahlung and double bremsstrahlung.

The irreducible background comes from direct production of photons either directly in a Born process or through different types of initial or final state radiation. Some examples of the processes are illustrated in fig. 6.4. While the calculations for the $\mathrm{H} \rightarrow \gamma\gamma$ branching ratio is performed quite precise with the main uncertainty from the value of α_s there are many theoretical uncertainties for the irreducible background with an uncertainty as high as 50% on the rate.

By simulating single electrons and photons with pile-up it has been shown in [18] that a rejection of 99.8% can be reached for electrons providing a total rejection of the $\mathrm{Z}^0 \rightarrow \mathrm{e}^+\mathrm{e}^-$ background of 250.000 and thus reducing it to 10% of the signal. The photon efficiency was shown to be 86% leading to a efficiency from the tracker alone of only 74% for $\mathrm{H} \rightarrow \gamma\gamma$. Many of the rejected photons are converted photons which are rejected by identification of the electron in the precision layers by the method used in [18]. The result is a major worry since the simulation was performed in the central rapidity region where there is a relative low amount of material in the tracker. At high rapidities the efficiency for photons will probably be even lower.

With the conversion algorithm described in section 5.7 a study was made to see if it is possible to recover the lost converted photons by finding the partners to the identified photons. For this a sample of 4.470 single electrons and 10.000 single photons with $p_{\mathrm{T}} = 50$ GeV were simulated at the same pseudorapidity $\eta = 0.3$ as the simulations in [18]. The layout of the inner detector was what was called the Panel layout and can be found documented in [19]. Of the photons 1108 of them had converted within the tracker.

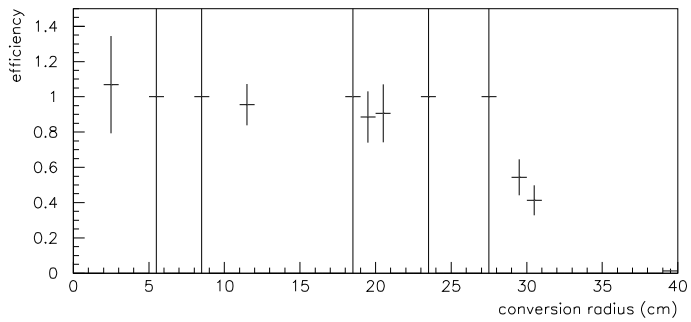

Figure 6.5: The efficiency for finding the tracks from a conversion at a given radius of conversion. The lower efficiency for track finding at larger radii is solely an effect of the pattern recognition not being optimised for conversions.

The present reconstruction program is only able to reconstruct tracks passing through most of the detector and hence will find tracks only from conversions if they converted within the silicon layers closest to the interaction point. The purpose of this analysis was not to look into pattern recognition problems but instead to make a first iteration of the usage of conversion identification in rejecting single electrons. Hence the efficiencies for finding conversions has been normalised to the number of events with tracks found by the Kalman filtering program. The efficiency for the pattern recognition can be seen in fig. 6.5 where the efficiency for finding the tracks from a conversion is plotted versus the conversion radius.

The identification criteria for conversions are

- **Xi2Kal** Maximal χ^2 per degree of freedom for the Kalman filters fit in the silicon layers.
- **TRT** Minimum number of hits on both tracks in the TRT
- **TR** Minimal fraction of TR hits to the total number of hits in the TRT on the track with the lowest p_{T} of the two.
- **dRecon** If R_{min_i} is the radius of the innermost hit on the tracks and R_{conver} the fitted radius from the vertex fit then

$$d_{\mathrm{Recon}} = |R_{\mathrm{conver}} - \max(R_{\mathrm{min}_1}, R_{\mathrm{min}_2})|. \tag{6.3}$$

- **MinRHit** The radius of the innermost hit on the two tracks.
- **Xi2Ver** Maximal χ^2 of the vertex fit

- **Xi2Mass** Maximal χ^2 of the zero mass constraint fit.
- **MinPt** Lowest p_T of tracks used in conversion candidates.
- **PtSumPri** Minimum p_T after the primary vertex constraint fit.

Xi2Kal and **TRT** are simply cuts on the track finding efficiency and have nothing to do with the actual conversion identification. **dRecon** uses the fact that the fitted vertex position is often far away from the innermost hit when an electron and a pile-up track are interpreted as a conversion. It is not given that it is optimal to reconstruct tracks down to the lowest limit of 0.5 GeV transverse momenta as the spectrum of pile-up tracks is strongly peaked at low p_T. The cut **PtSumPri** is similar to the variable R in (6.2) since the particles are simulated at a fixed transverse momenta and will be applied in any case for the γ/π^0 separation following the identification of the conversions.

The efficiency of the different cuts are shown in fig. 6.6. It can be seen that a rejection of only $0.6 \pm 0.1\%$ is reached, far from the criteria of 0.2% for electrons, and already the efficiency for the converted photons in the layers at 10 and 20 cm is down at 60%. If the electron efficiency is forced down to $0.2 \pm 0.06\%$ the corresponding efficiency for converted photons is as low as 30%. It is seen that even with use of both the transition radiation from the electrons and a vertexing algorithm it is not possible to save the photons which convert in the beampipe or the layer closest to the interaction point at 10 cm.

If conversions in the beampipe and the innnermost layer are ignored by setting **dRecon** to 15 cm the situation looks much better. Here the electron efficiency of $0.17 \pm 0.06\%$ can be reached with an efficiency for photons converted at 20 cm of 75% which can be regarded as quite satisfactory and encourage further simulations in the most recent design of the inner detector and in the full pseudorapidity coverage. The cut **TR**$= 0.10$ on the transition radiation is essential to reach the quoted efficiencies.

6.3 Inclusive electron identification

With inclusive electrons is meant the identification of high p_T isolated electrons independent of the creation process. As all interesting physics processes involving electrons are subsamples of inclusive electrons the identification efficiency and background rates are of extreme importance. Also all the inclusive electrons can be of interest for calibration of the calorimeter as described

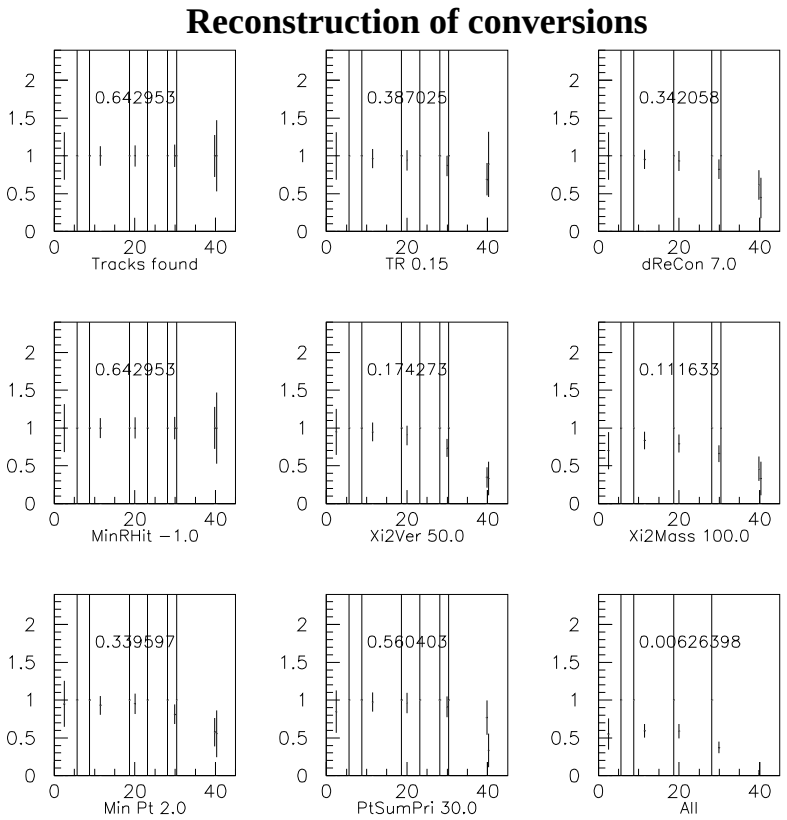

Figure 6.6: The efficiency of the individual cuts for rejecting single electrons by identification of conversions. In each small figure the name of the cut is written below with the value following directly afterwards. The errorbars are the efficiency for identifying converted photons at the given radius of conversion measured in cm. On the figure is written the efficiency for identifying electrons with this cut only. The last figure shows the effect of all cuts applied simultaneously.

in section 6.4 and to make internal checks on the electron efficiency for the complete detector.

As already mentioned in chapter 2 the background from QCD jets is in the physics processes about a factor 10^5 above the rate of inclusive electrons with $p_{\mathrm{T}} > 20$ GeV. To get numbers on the rejection factor for the jets a sample of 10^6 jets was simulated in a now very historic design of the ATLAS detector.

Process	Rate (s^{-1})	Rate (s^{-1}) TR + conversions found
jet with electron	106 ± 33	95 ± 29
jet with hadron	136 ± 37	< 10
jet with conversion	75 ± 26	< 10

Table 6.1: The rate of events identified as isolated electrons in the detector at the full luminosity $L = 10^{34}\mathrm{cm}^{-2}\mathrm{s}^{-1}$. The third column represent the results expected after transition radiation has been used to reject hadrons and conversions have been identified. The limited statistics prevented this from being done on the jet sample itself.

The complete chain of identification criteria planned for ATLAS has been applied to the jets.

- A cluster with $E_{\mathrm{T}} > 17$ GeV in a $(\eta \times \varphi) = (3 \times 7)$ window in the electromagnetic calorimeter. The window size is measured in units of the calorimeter granularity.
- Leakage to the hadronic calorimeter behind the cluster below 0.5 GeV.
- An isolated cluster defined as

$$\frac{E_{\mathrm{T}}(\eta \times \varphi = 7 \times 7) - E_{\mathrm{T}}(\eta \times \varphi = 3 \times 7)}{E_{\mathrm{T}}(\eta \times \varphi = 7 \times 7)} < 0.10. \tag{6.4}$$

- A requirement of a narrow energy profile in the η direction of the preshower.
- A track found in the inner detector pointing towards the cluster and with

$$0.7 < \frac{E_{\mathrm{T}}}{p_{\mathrm{T}}} < 1.4. \tag{6.5}$$

In the jet sample three groups of almost equal size survive all identification criteria above. The first group is composed of real electrons mainly from semileptonic decays of heavy quarks and leptonic decays of Z^0 bosons. The second group is hadrons faking an electron in the calorimeter by having an early shower development and the third group is reconstructed electrons from conversions with the photons mainly from π^0 decays. Details on the simulation and the rejection process can be found in [20]. At this point the background outnumbers the inclusive electrons by a factor two thus only one in every three electrons identified in ATLAS would really be an electron as seen in the second column of table 6.1. An independent analysis of single simulated electrons in [20] have a total efficiency of electrons of $65.2 \pm 1.0\%$ when all the jet rejection cuts are applied.

While the interest is to keep the electrons, the two other groups can be rejected further by making full use of the inner detector. The hadrons can be rejected using a cut on the amount of transition radiation on the tracks. As shown in [12] no jets in the final hadron group survive the electron identification criteria and this sets an upper limit of $10\,\mathrm{s}^{-1}$ on the background rate from hadrons above 20 GeV at full luminosity.

The program developed for identifying conversions in the $H \rightarrow \gamma\gamma$ decay has also been used on the group of suspected conversions. Two tracks of opposite charge and with p_T above 0.5 GeV/c are found in a region of interest around the electromagnetic cluster in 21 of the 39 jets in this group. 11 of the events survive the cut of above 10% transition radiation hits on each track and cuts on the quality of the vertex and mass constraint fit as in section 6.2. At a first sight it looks very bad if only a third of the conversions can be reconstructed but such a conclusion cannot be drawn from the simulated data. The very large jet sample was simulated without storage of information on conversions and hence there is no guaranty that the selected events searched for conversions have conversions at all. The only information is that the particle of highest p_T close to the cluster in the calorimeter is a photon.

The sample of electrons and photons with pile-up used for the $Z^0 \rightarrow e^+e^-$ rejection analysis have been optimised for high photon efficiency instead. For the conversions at 10 and 20 cm an efficiency of 89% was achieved using a cut on the fraction of transition radiation hits of 0.10 on the lowest p_T track. Only 3.8% of the electrons were accepted as conversions and thereby lost in the sample of electrons. It can be seen that the results disagree by almost a factor 3 with the results obtained from reconstruction of conversions in the jet sample. With the next simulations of 10^7 jets planned information on conversions will be stored making it possible to perform a detailed analysis on the jets themselves.

Assuming the result of an identification efficiency of 90% for conversions and above a factor 10 rejection of hadrons the rates in the right part of table 6.1 can be reached making the real electrons outnumber the fake electrons by a factor 5 in inclusive electrons.

With the uncertainty in the crosssection for production of b-quarks and also large uncertainties in the charge exchanging effects involved in pions faking electrons in the calorimeter the increased rejection provided by the inner detector is essential to provide a safety margin for a working electron identification in ATLAS.

6.4 Calibration of the EM calorimeter

Calibration of the electromagnetic calorimeter is an important subject where a clean sample of inclusive electrons can prove essential. To evaluate the problem a small toy Monte Carlo has been developed. The calibration set the scale of the energy measurement and hence errors in the calibration is the source of the constant term B in the energy resolution

$$\frac{\sigma(E)}{E} = \frac{\mathrm{A}}{\sqrt{E}} \oplus \mathrm{B} \tag{6.6}$$

At low energy this is of no relevance compared to the sampling term A but at high energies it will become the dominant term. The performance goal for ATLAS requires a constant term of 0.7%.

What is meant by calibration of the calorimeter is to find correction factors such that $E/p = 1$ in mean on both a local (cell to cell) scale and on a global scale. E is here the energy measured in the calorimetric cluster at the point where the track of momenta p hits the calorimeter.

Electrons for the calibration can be either inclusive electrons or electrons identified from a specific physics process like $\mathrm{Z} \rightarrow \mathrm{e}^+\mathrm{e}^-$ or $\mathrm{W} \rightarrow \mathrm{e}\nu$. A description of inclusive electrons can be found in section 6.3. The specific physics processes has the advantage of constraints on the measurement of the momenta but they suffer from much lower cross section. Also there is not planned any specific trigger for Z^0 events.

6.4.1 The toy Monte Carlo

This very simple model simulates the spectrum for a calibration using inclusive electrons.

For the electrons the model simulates the E_{true}/p spectrum of reconstructed electrons as given for 20 GeV electrons after a bremsstrahlung recovery. Together with the other simulated spectra this can be seen in fig. 6.7.

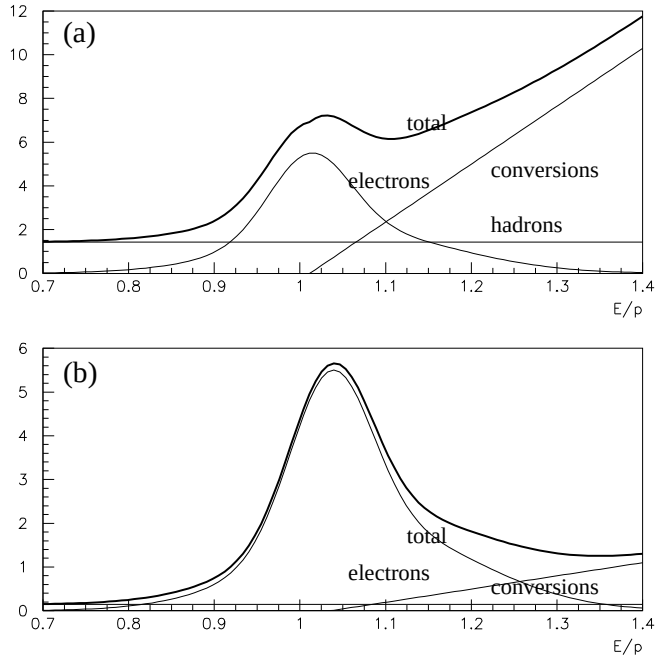

Figure 6.7: The E/p spectrum used for the calibration of the electromagnetic calorimeter. In (a) without the use of the TRT and in (b) with.

The width of the Gaussian peak and the shape of the bremsstrahlung tail has been made to approximate the spectrum given in fig. 3.36 in the ATLAS Technical Proposal [1].

The backgrounds to inclusive electrons are discussed in section 6.3. Keeping the interval $0.7 < E/p < 1.4$, the spectrum from non rejected hadrons is assumed to be flat, because we are far out on the tail of the E/p distribution of hadrons in the electromagnetic calorimeter. The background from conversions can on the other hand not be assumed to be flat at all. The conversions are from prompt photons and π^0 decays. In both cases the background is from events where only one of the two (or more) tracks are identified leading to $E/p > 1$. The spectrum here is assumed to rise linearly from $E/p = 1$ as can be seen in fig. 6.7.

A fixed number of events is now simulated according to the theoretical distribution and a χ^2 fit made of the form

$$\text{fit(x)} \quad = \quad A \text{ elec} + B \text{ hadron} + C \text{ conver} \tag{6.7}$$

$$
\begin{aligned}
\text{elec} &= (1 - \mathrm{b_{frac}})\mathrm{N}(\mu, \sigma) + \mathrm{b_{frac}}\mathrm{N}(\mu, \sigma_{brem}) \\
\text{hadron} &= \frac{1}{h - l} \\
\text{conver} &= \begin{cases} 0 & \mathrm{x} < \mu \\ \frac{2(x-\mu)}{(h-\mu)^2} & \mathrm{x} > \mu \end{cases}
\end{aligned}
$$

with μ, A, B, C as variable parameters and the remaining parameters assumed known in advance. $l = 0.7$ and $h = 1.4$ are the low and the high limits of the region used in E/p.

A nice and quite detailed description of calibration using inclusive electrons at the CDF detector can be found in [21] where a total sample of 17.000 electrons give a constant term of 1.7% for the individual cells. Before comparing remember that the e/jet rate is much lower at LHC compared to the Tevatron $\mathrm{p\bar{p}}$ collider.

6.4.2 Time for calibration

The time needed to make a calibration is given by the number of electrons required to hit each cell. In fig. 6.8 is seen a simulation with 750 electron events and the subsequent fit both with and without the TRT used to reject hadrons and conversions.

Not to be limited by statistics, the accuracy of the fit needs to be better than the required accuracy of the overall constant term. To obtain an overall constant term of 0.6% M. Lefebvre has in [22] estimated a local constant term of 0.4% to be needed. In fig. 6.9 the accuracy of the fit can be seen as a function of the number of inclusive electrons in a cell. As expected the precision scales with the square root of the points in the fit.

With a calorimeter cell size of $(\Delta\varphi \times \Delta\eta) = (0.025 \times 0.025)$ and the rates from table 6.1 in a coverage of $(\varphi \times \eta) = (2\pi \times 6)$ the rates in a single cell will be approximately 50000 times smaller. This assumes a uniform distribution in η of inclusive electrons which is approximately correct. At high luminosity $\mathrm{L} = 10^{34}\mathrm{cm}^{-2}\mathrm{s}^{-1}$ a statistical accuracy of 0.4% will be reached after 375000 s (5 days) with the use of the inner detector and especially the TRT, and the double time without. At low luminosity the calibration time will be 10 times longer in both cases.

An electromagnetic cluster covers more than one cell in the calorimeter. Hence the cells can not be calibrated independently and a sliding window technique is required, where one cell is taken together with different cells in the neighbourhood.

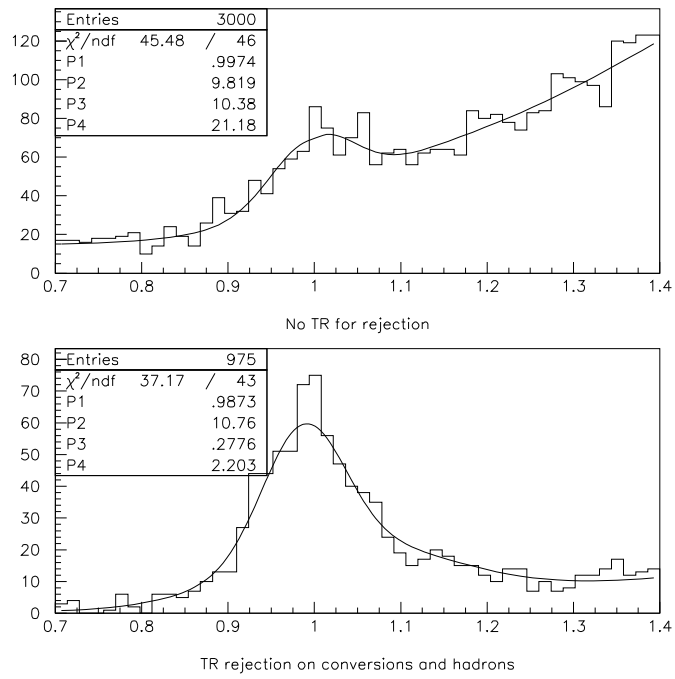

Figure 6.8: 750 electrons simulated with the background for inclusive electrons. The situation before use of the TRT (a) and after transition radiation is used to reject hadrons and conversions (b). The fit has the levels of background as free parameters but the shape is taken as fixed

6.5 b-tagging in $\mathrm{H} \rightarrow \mathrm{b}\bar{\mathrm{b}}$ decays and top jets

By b-tagging is meant the process of identifying QCD jets containing a bottom quark. B physics and b-tagging should be sharply distinguished. In B physics one is concerned with specific reconstruction of final states from B-mesons or B-baryons. The typical energy scale here is $p_{\mathrm{T}} < 15$ GeV/c. In b-tagging one is interested in physics where heavy particles decay into states with several jets containing b-quarks. Since the initial particle is heavy the energy scale will be high with jet energies of 40 GeV or above.

There are 2 main methods for b-tagging.

- Secondary vertex tagging where during reconstruction it is found that not all particles point back to one primary vertex, but some instead from a secondary vertex displaced by a small distance. B-mesons lifetime around 1.5 ps give decay distances of the order of several mm

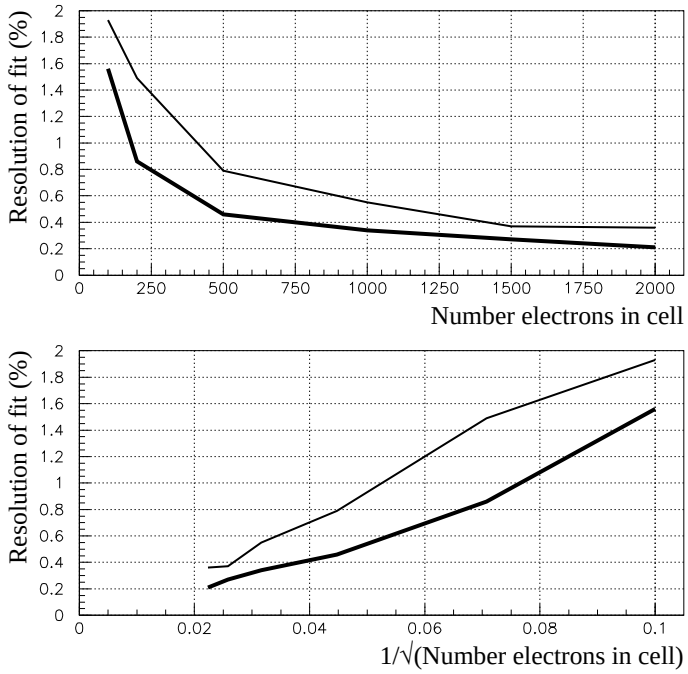

Figure 6.9: The precision of the fit for calibration of the EM calorimeter. On top the resolution in percent versus the number of signal events in each cell. In the bottom frame can be seen the expected $1/\sqrt{n}$ proportionality in the fit. In both plots the light line is without the use of the inner detector and the heavy line with the inner detector used to reject hadrons and conversions.

and it is at the decay point of the B-meson that a secondary vertex is found. Especially jets with only u,d and s quarks will be rejected very efficiently by identification of secondary vertices. Also some rejection power is achieved against jets with c-quarks since the lifetimes for $D^{\pm}$ and D^{0} are 1.0ps and 0.5ps respectively. Hence the D-mesons will decay closer to the primary vertex and the probability for identifying a secondary vertex is lower compared to the same probability for B-mesons.

- For the lepton tag is used the fact that B-mesons can decay to leptons through semileptonic decays. The identification of the lepton can provide identification of jets with B-mesons and rejection against jets with lighter quarks.

Since it is in the lepton tag that electron identification is of importance, only the lepton tag will be considered in this section. The idea is to identify leptons down to as low a transverse momentum as possible. If a lepton is found the closest jet is identified as a b-jet.

Decay product from X_b	Branching ratio (%)
$X_c e^- \nu$	8.2
$X_c \mu^- \nu$	6.3
$X_c \to X_s e^+ \nu$	4.3
$X_c \to X_s \mu^+ \nu$	0.9
$X_c e^- \nu \to X_s e^- \nu e^+ \nu$	1.1
$X_c \mu^- \nu \to X_s \mu^- \nu \mu^+ \nu$	0.6
$X_c e^- \nu \to X_s e^- \nu \mu^+ \nu$	0.7
$X_c \mu^- \nu \to X_s \mu^- \nu e^+ \nu$	1.0
Xe	15.3
$X\mu$	9.5
$X(e/\mu)$	23.1

Table 6.2: The different semileptonic decays of B-mesons. Branching ratios are listed both for direct and indirect decays containing an electron with p_T above 2 GeV/c or a muon with $p_T > 5$ GeV/c. X_q denotes any hadronic state containing a quark of type q. The branching ratios are from the latest PDG data and the kinematical spectra of the leptons taken from a simulation of $H \to b\bar{b}$.

B-mesons have a lepton among the decay products in several different decays. All the different possibilities are listed in table 6.2 where it has been taken into account that only leptons above a certain threshold in p_T can be identified.

To reach a low threshold in lepton identification requires special attention. Muons below 5 GeV/c will often not penetrate the hadron calorimeter and the signal from the last compartments of the calorimeter has to be included in the search for muons. This has been investigated in [23].

For electrons using only the electromagnetic calorimeter the efficiency for electron identification drops sharply at p_T below 5 GeV/c as shown in [24] and below 2 GeV/c no identification power is left. Using the TRT however should make it possible to extend the p_T range down to 1 GeV/c for electron identification. A lower threshold will not improve significantly on the efficiency for direct semileptonic decays $X_b \to X_c e^- \nu$ where 90% of the electrons have $p_T > 2$ GeV/c but for the cascade decay $X_b \to X_c \to X_s e^+ \nu$ where the

same fraction is only 55%, there will be a major gain in lowering the threshold to 1 GeV/c. The preliminary study done in [24] not using the TRT for electron identification gives a lower bound on the b-tagging efficiency from electrons $\varepsilon_b^e = 10\%$ with a rejection factor against light quark and gluon jets of 50. The p_T spectra used are from a simulation of $H \to b\bar{b}$ at LHC for a Higgs mass of 100 GeV.

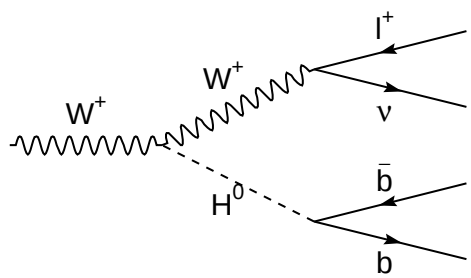

Figure 6.10: Associative production of a Higgs scalar in connection with a W boson. The Higgs is identified through a trigger on a semileptonic decay of the W and the Higgs decaying into a pair of bottom quarks.

It has already been seen that the detection of a low mass Higgs in the $H \to \gamma\gamma$ channel is extremely difficult, and being able to observe the Higgs in other decay modes could be a major help in identifying the Higgs. The dominant decay of a Higgs below the mass where it can decay to two Z bosons is $H \to b\bar{b}$. To observe the production of the Higgs and the decay through $H \to b\bar{b}$ directly is however impossible due to the irreducible background from the 1000 times higher production rate of Z with branching ratio into $b\bar{b}$ pairs of 15%. Instead the associative production of a Higgs in connection with a W as shown in fig. 6.10 is a promising decay.

In certain Supersymmetric extensions of the standard model the branching ratio of the H^0/h^0 to two photons decay is suppressed with respect to the standard model Higgs and a detection in the $H \to b\bar{b}$ channel will be the only possibility.

The backgrounds for associative Higgs production has been studied in [25] leading to the results in table 6.3 for a simulated Higgs mass of 100 GeV. Recent studies [26] on b-tagging are very encouraging and it seems that an efficiency for b-tagging can be kept at 50% with a rejection of a factor 50 against non-charm jets. The study on b-tagging was done using only the secondary vertexing method and, since the two methods are independent a total b-tagging efficiency of

$$\varepsilon_b = \varepsilon_b^{\text{vertex}} + (1 - \varepsilon_b^{\text{vertex}})\varepsilon_b^{\text{lepton}} \approx 60\% \tag{6.8}$$

Process	Rate	$R = 100$ $\varepsilon_b = 30\%$	$R = 50$ $\varepsilon_b = 50\%$
WH	$440\varepsilon_b^2$	40	110
WZ	$600\varepsilon_b^2$	54	150
$\mathrm{Wb\bar{b}}$	$3660\varepsilon_b^2$	330	910
$\mathrm{q\bar{q}} \rightarrow \mathrm{t\bar{b}}$	$570\varepsilon_b^2$	50	140
$\mathrm{t\bar{t}}$	$5140\varepsilon_b^2$	470	1290
$\mathrm{qg} \rightarrow \mathrm{t\bar{b}}q$	$210\varepsilon_b^2$	20	50
Wjj	$5.3 \cdot 10^6 1/R^2$	530	2130
Wjb	$4.1 \cdot 10^4 \varepsilon_b/R$	120	410

Table 6.3: The rates for production of associative Higgs and the dominant backgrounds at an integrated luminosity of $10^4\mathrm{pb}^{-1}$ and a simulated Higgs mass of 100 GeV. Two different efficiencies for b-tagging are assumed. In recent analysis on b-tagging it seems likely that even the efficiency of 50% can be exceeded. From [25].

assuming a b-tagging efficiency using lepton tag from electrons and muons of 10% each.

It can be seen from table 6.3 that even being optimistic and assuming a b-tagging efficiency of 60% the identification of a 100 GeV Higgs will still be extremely difficult. One years of datataking with an integrated luminosity of $10^4\mathrm{pb}^{-1}$ will give a significance $\mathrm{S}/\sqrt{\mathrm{B}}$ of 2.0. Hence an identification of the Higgs in only the $\mathrm{H} \rightarrow \mathrm{b\bar{b}}$ channel will not be possible. However together with the similar channel of associated Higgs production with $\mathrm{t\bar{t}}$ pairs an identification after a few years of LHC running at low luminosity will be reachable.

With a Higgs mass changing from 80 to 120 GeV the predicted cross section for associated production drops a factor 4 while the backgrounds stay almost constant according to [25]. So for a light Higgs down to the discovery limit of LEP2 the situation looks good, but in the range from 100 to 120 GeV of the Higgs mass the two photon channel will be the only possibility.

How b-tagging will work at high luminosity is not known at the moment. Very preliminary results look optimistic for the secondary vertex tagging method.

B-tagging will be very important for all physics with top quarks since top quarks almost entirely will decay to b-quarks. A double b-tag on both top quarks in the production of $t\bar{t}$ pairs together with a high p_{T} isolated lepton from the decay $t \rightarrow bl\nu$ will be a good selection criteria for top quarks.

Chapter 7

Conclusion

The aspects of electron identification in a detector at LHC have been presented, both through analysis of data from a prototype of the Transition Radiation Tracker, and through simulations of specific physics channels where electron identification is a key issue.

The analysis of data from the prototype of the endcap TRT showed a detector performing very well for separating electrons and pions. With a detector length of 780 mm a pion efficiency of 0.6% was achieved keeping the electron efficiency at 90%. The very strong dependence between detector length of the TRT and detection efficiency of pions was experimentally proven.

A program for identifying converted photons in the inner detector using the Kalman filtering technique was developed. It was used to evaluate the effect conversions have on detection of the decay of a Higgs scalar to two photons. The program was also used to identify conversions identified by the tracker and calorimeter as inclusive electrons. This first version of the program performs very well but need to be enlarged into a package identifying photons converting in all parts of the inner detector.

In the chapter on the physics potential of electron identification it was proven that rejection of the background from QCD jets requires better particle identification than the calorimeters can provide. The TRT provides the addtional rejection power and is at the same time an important part of the pattern recognition and track fitting in the inner detextor. The combination of a silicon tracker and the TRT improves the rejection of QCD jets by a factor of 10. The hadron and conversions identification are of almost equal importance.

For the B-physics the level 2 trigger on J/Ψ decaying to electrons is only possible with the use of the electron identification in the TRT. Without the TRT information used at level 2 only the decay to muons can be used.

The time used for calibration of the electromagnetic calorimeter can be considerable reduced using the additional rejection of hadrons and conversions provided by the TRT. Especially at low luminosity this will be important.

In the future I will try to connect the testbeam analysis and the physics simulations stronger. The conversion algorithm will be applied to the testbeam data and the simulation of the TRT will be tried out on the testbeam setup. For the analysis of a possible $H \rightarrow \gamma\gamma$ decay the work on conversions will be extended to the analysis of γ/π^0 separation which has never before been analysed using a realistic identification of conversions.

Appendix A

Glossary

B-tagging Identification of jets containing baryons with b-quarks.

BC Beam chambers placed in the testbeam to make the external measurement of the track parameters. Gaseous detectors with an approximate precision of 400μ in both coordinates.

DAQ Data acquisition

DTMROC Drift time measuring read out chip. The chip mounted directly on the TRT which measures the drift time in the straws and keeps the results in a buffer until they are required by a level 1 trigger.

ID The ATLAS Inner Detector.

LEP The electron-positron storage ring at CERN.

Lx Trigger level x.

MC Monte Carlo. Computer simulations of physics events and the detector response.

PE Polyethene. Polyethene is compared to polypropylene far more radiation hard.

PP Polypropylene.

p_{T} Always momenta of a particle transverse to the beam axis, never momenta transverse to a jet axis as often used with LEP physics.

RD6 The R&D collaboration at CERN working with the development of transition radiation detectors for physics at hadron colliders. The collaboration transforms gradually into the ATLAS TRT group.

Rapidity In many places used wrongly as a short form of the pseudo rapidity defined as

$$\eta = -\log \tan \frac{\theta}{2}.$$

However at high p_{T} the pseudo rapidity and the rapidity are equal.

RoI Regions of Interest. The level 1 trigger system will point out special areas of the detector where the level 2 system will look for the signatures of interesting events.

TP The ATLAS technical proposal.

TRDA The chip for shaping and discriminating on thresholds mounted on the testbeam setup 1995. The TRDA will be replaced with the ASD chip developed for the SDC detector.

TRDS Transition radiation detector support chip. Controls dead channels and sets the levels for the discriminators to low and high threshold. In future versions of the readout electronics the functions of the TRDS will be incorporated in the DTMROC.

TRT The Transition Radiation Tracker.

TRT The transition radiation tracker for ATLAS.

TR Transition radiation. TR hits are the hits passing the high threshold in the read out system of the straws.

Bibliography

[1] The ATLAS collaboration. ATLAS technical proposal. Technical Report CERN/LHCC/94-43, CERN, December 1994.

[2] N. Ellis and M. B. Gavela, editors. *1993 European School of High-Energy Physics*, number CERN 94-04. CERN, September 1993. Future Research in High Energy Physics, G. Flügge.

[3] X. Artru, G.B. Yodh, and G. Mennessier. Practical theory of the multilayered transition radiation detector. *Physical Review D*, 12(5):1289–1306, 1975.

[4] L. Fayard, editor. *Transition Radiation*, volume LAL-88-55, November 1988. Lectures given at l'Ecole Joliot Curie 1988, Carcans, France, September 26-30, 1988.

[5] Boris Dolgoshein. Transition radiation detectors and particle identification. *Nuclear Instruments and Methods in Physics Research*, A252:137–144, 1986.

[6] Boris Dolgoshein. Transition radiation detectors. *Nuclear Instruments and Methods in Physics Research*, A326:434–469, 1993.

[7] Edwin A. Uehling. Penetration of heavy charged particles in matter. *Annual review of nuclear science*, 4:315, 1954.

[8] H. U. Bengtson and T. Sjöstrand. Pythia. *Computer Physics Commun.*, 46:43, 1987.

[9] CERN, Theory division. PYTHIA *5.6 and* JETSET *7.3 Physics and Manual*, CERN-TH.6488/92 edition, September 1992.

[10] CN division Application Software Group. *GEANT Detector Description and Simulation Tool.* CERN, ver. 3.15 edition, 1993.

[11] Igor Gavrilenko. Pattern recognition in TRD/Tracker (TRD/T). ATLAS Internal note INDET-NO-016[1], October 1992.

[12] U. Egede, T. Åkesson, D. Froidevaux, and I. Gavrilenko. Fake Tracks in the ATLAS Straw Detector. ATLAS Internal note INDET-NO-082, December 1994.

[13] R. K. Bock et al. *Data Analysis Techniques for High Energy Physics Experiments*, chapter 3. Cambridge University Press, 1990.

[14] R. Frühwirth. Application of Kalman filtering to track and vertex fitting. *Nuclear Instruments and Methods in Physics Research*, A262:444–450, 1987.

[15] Thomas Lohse. Vertex Reconstruction and Fitting. ftp://x4u2.desy.de/pub/herab/vertex/vertex.ps, 1995.

[16] Mária Smižanská. Second Level TRT Trigger for B-Physics. ATLAS Internal note PHYS-NO-XXX, 1996.

[17] D. Froidevaux et al. Simulation and optimization of the ATLAS electromagnetic calorimeter: γ/π^0 separation. ATLAS Internal note CAL-NO-072, February 1995.

[18] Silvia Schuh. Higgs hunting with a transition radiation tracker. Master's thesis, Institut für Kernphysik, Technische Universitüt Wien, May 1995.

[19] A. Fox-Murphy, R. Nickerson, and T. Weidberg. ATLAS internal note INDET-NO-043, March 1994.

[20] T. Pal et al. Inclusive electron identification and QCD-jet rejection in the ATLAS detector. ATLAS Internal note INDET-NO-127, April 1996.

[21] CDF collaboration. Measurement of the W-boson mass in 1.8-TeV $\bar{p}p$ collisions. *Physical Review*, D43(7):2070–2093, 1991.

[22] Michel Lefebvre. Some thoughts on cell-to-cell calibration. Transparencies presented at the physics ATLAS workshop in Trest, June 1995.

[23] J. Budagov, D. Pantea, M. Bosmas, and M. Nessi. Low p_{T} muons in b-jets in ATLAS Tilecal. ATLAS Internal note TILE-NO-062, September 1995.

[1] All ATLAS internal notes are available through WWW at the address http://atlasinfo.cern.ch/Atlas/GROUPS/notes.html

[24] Fabiola Gianotti. Tagging of low-p_T electrons from b decays with the ATLAS electromagnetic calorimeter. ATLAS Internal note PHYS-NO-049, March 1995.

[25] Daniel Froidevaux and Elzbieta Richter-Was. Is the channel $H \to b\bar{b}$ observable at LHC. ATLAS Internal note PHYS-NO-043, September 1994.

[26] I. Gavrilenko, S. Haywood, A. G. Clark, D. Froidevaux, and L. Rossi. Present status of b-tagging studies in ATLAS. ATLAS Internal note INDET-NO-115, November 1995.